Available online at www.sciencedirect.com
SCIENCE DIRECT®
Thermochimica Acta 433 (2005) 27–50
thermochimica acta
www.elsevier.com/locate/tca

Thermoporometry by differential scanning calorimetry: experimental considerations and applications

Michael R. Landry *

Eastman Kodak Company, Research and Development Laboratories, 1669 Lake Avenue, Rochester, NY 14650-2132, USA

Received 2 December 2004; received in revised form 8 February 2005; accepted 10 February 2005
Available online 7 March 2005

Abstract

Thermoporometry is a calorimetric method for characterizing pore structure from the melting or freezing point depression of a liquid confined in a pore, by reason of the added contribution of surface curvature to the phase-transition free energy. A summary of the theory behind the technique is provided, and a thorough evaluation of the technique using a laboratory DSC instrument is presented. Experimental protocols are described for the examination of mesoporous solids, specifically, controlled-pore glass standards. In addition to water, several organic liquids have been also used, including chlorobenzene, cyclohexane, and 1,4-dioxane. Pore radii as large as 1000 nm may be quantitatively measured with appropriate experimental conditions. Methods for obtaining total pore volume, specific surface area, pore radius, and pore size distributions are discussed and compared to Hg intrusion results. The report concludes with applications of thermoporometry toward the characterization of inorganic particles, porous organic beads, and the pore structure in coated media.

Keywords: Thermoporometry; Controlled-pore glass; Mesoporous materials; Pore size distribution; Porosity

1. Introduction

Porosity is the ratio of the void or interstitial volume of a material to its mass. The voids comprise holes and cracks within a material that create an inner surface. For a coated layer, these pores may be entirely closed or open, the latter having a channel that connects with the surface. Porosity is also used to characterize particulate matter; thus a porous structure can be contained within a particle (intraparticle), or created by the open space between particles (interparticle), such as for an ensemble of solid spheres. In general, materials can be made porous by a combination of both intraparticle and interparticle porosity. It is useful to know what fraction of interstices is available to a penetrating liquid. Unfavorable wetting of porous addenda may preclude their ability to imbibe a liquid; therefore, a pore volume measurement alone, such as from mercury intrusion or nitrogen adsorption, may not be entirely meaningful. Other characteristics that might be relevant are the average pore size, the pore size distribution, the size of a pore "throat", that is, the entrance channel to a pore, a generalized pore shape (e.g., cylindrical, spherical, slit, etc.), surface area, and tortuosity. When classifying pores according to size, three general categories are used [1]: micropores are the smallest, usually falling below 2 nm in diameter; mesopores have diameters roughly between 2 and 50 nm; and macropores are considered 50 nm and greater. Using these broad classifications, mesopores and macropores are likely to be the most effective with respect to fluid absorption.

A recent series of publications give excellent reviews of porous structure measurements for porous particles [2] and membranes [3,4]. Analytical methods are as varied as microscopy (electron transmission, scanning, optical), X-ray scattering, and liquid intrusion (mercury porosimetry, nitrogen adsorption/desorption, thermoporometry). In the following text, the essence of the intrusion techniques is summarized along with caveats about the utility of these methods. Significant detail is devoted to thermoporometry, a porosity characterization method that utilizes the traditional differential scanning calorimetry technique in an untraditional manner. The thermodynamic principles

* Tel.: +1 585 722 5878; fax: +1 585 477 7781.
E-mail address: michael.landry@kodak.com.

0040-6031/$ – see front matter © 2005 Elsevier B.V. All rights reserved.
doi:10.1016/j.tca.2005.02.015

governing thermoporometry are covered. Much of the experimental work herein is for well-characterized porosity size standards, controlled-pore glass (CPG). Ultimately, the thermoporometry data should compare favorably to those taken by the more traditional N_2 adsorption/desorption and Hg intrusion methods on the same materials.

1.1. Mercury intrusion and nitrogen adsorption methods

Quantitative information about a porous material such as mean pore size, pore size distribution, and total pore volume may be obtained from the pore-filling methods of mercury intrusion–extrusion and nitrogen adsorption/desorption manometry. The specific surface area of a material is determined by gas adsorption at relatively low pressures using the BET (Brunauer, Emmett, Teller) theory for multilayer adsorption. Both techniques in the pore-filling regime are based on surface tension, capillary forces, and pressure to derive information about porosity. The uptake of liquid into or the expulsion out of porous media depends on the external pressure of the probing liquid. For nitrogen adsorption, the smallest pores are filled at the lowest pressures, whereas for mercury intrusion, the largest pores are filled at the lowest pressures. Each method also is able to measure the total pore volume and specific surface area of a material without resorting to an explicit pore shape model. Because of the upper limit of pore size accessible to N_2 adsorption, any pore volume due to large pores, may be missed entirely. Nevertheless, for porous materials having a pore size range detectable by both methods, there is usually close agreement in terms of total pore volume; on the other hand, surface area tends to be larger when measured by gas adsorption [5].

With mercury porosimetry, mercury is added to an evacuated cell and forced into pores and voids by applying pressure. Care must be taken that the sample is dry, because mercury will not displace liquid already in the pores. This could present a disadvantage when characterizing hydrophilic samples. Another concern is the possibility that high mercury pressures may crush or otherwise deform a pore. This concern is especially important when trying to accurately measure the pore volume of soft material, such as paper or membrane media. The use of mercury or liquid nitrogen for a probe liquid is merely for the purpose of obtaining pore size and volume information; neither liquid would be expected to interact with either a porous filler or coating intended to absorb "traditional" liquids, such as water or organic solvents.

Despite these minor reservations, the intrusion and adsorption porosimetry methods have proven to be useful, not only for measuring total pore volume and surface areas, but also for measuring mean pore diameters and pore size distributions with the use of reasonable geometric models for pore structure. The techniques are considered acceptable for defining specifications in patent claims and for quality control purposes. They are capable of providing highly reproducible data, often to within a few percent. Commercial instruments and accompanying software for quantitative data analysis of porosity are available—both factors having significant relevance for any characterization effort. Therefore, both methods continue to be critical for porosity measurement.

1.2. Thermoporometry

Thermoporometry, also known as thermoporosimetry, is a calorimetric method that determines pore size based on the melting or crystallization point depression of a liquid confined in a pore [6]. A differential scanning calorimeter (DSC) is aptly suited for precise measurement of the relatively small temperature shifts because of particular sensitivity to exothermic freezing and endothermic melting transitions. The physical basis for the shift is that the equilibrium temperature for a solid–liquid phase transition is determined by the radius of curvature of the interface between the solid and liquid phases [7]. A liquid held inside a porous material is finely divided; therefore, the radius of curvature is closely related to the pore size. Experimental observations of water [6,8–11], organic liquids [6,12–16], molecular oxygen [17], and indium metal [18] reveal a reciprocal dependence between the melt temperature depression ΔT_m (or freezing temperature depression ΔT_f) and the nominal pore radius.

In general, no extraordinary sample preparation steps are required with thermoporometry. Water is a common probe liquid, which is relevant for examining materials and coatings designed specifically to absorb aqueous solutions. Another advantage to using water is that its heat of fusion, $\Delta H_f = 334$ J/g, is up to an order of magnitude larger than most organic liquids. The large ΔH_f of water enhances the sensitivity of the DSC technique to small volumes of adsorbed liquid.

The primary disadvantage of the method is that it is nontraditional, and its use is not as widespread as the gas adsorption and mercury intrusion methods. The effect of specific interactions between the probe liquid and the porous solid are largely unknown and may lead to uncertain interpretation of calorimetric signals. The technique has been promoted [6,19,20] as being able to determine pore size distributions if temperature dependence of physical parameters such as surface tension, contact angle, heat of fusion, and specific volume are known a priori. However, literature values for these parameters usually vary, leading to difficulty in the direct transformation of calorimetry curves into absolute pore size distributions. Thus experimental work often resorts to the use of reference materials that have been carefully measured by other methods, such as mercury intrusion or nitrogen adsorption, to calibrate for pore size determination.

1.3. Theoretical principles of porometry vis-à-vis pore size

The theoretical foundation of any porometry technique starts with an awareness of the interrelationship between the solid, liquid, and gas interfaces and the equilibrium state of a pure substance [6,7]. Surface tension becomes particularly

important for capillary systems when balancing mechanical, thermal, and chemical potential changes in transition from one phase to another, such as from gas to liquid or liquid to solid. Examples of capillary systems include high surface area colloidal particles, an aerosol mist of liquid droplets, micelles, vesicles, and small channels filled with liquids, such as a porous coating. The same thermodynamic principles apply for thermoporometry, nitrogen adsorption, and mercury intrusion methods when determining pore sizes.

The role of surface (or interfacial) tension is illustrated for a sessile liquid drop on an inert surface in equilibrium with its gaseous phase. By definition, equilibrium means that the exchange of molecules between the gas and liquid phases is such that the drop volume remains constant, and that the liquid and gas pressures, P_l and P_g, respectively, are uniform in each phase. For mechanical equilibrium to exist, the pressure difference across the gas/liquid surface $P_\mathrm{l} - P_\mathrm{g}$ is balanced by the gas–liquid interfacial tension γ_gl acting tangentially along the gas/liquid interface. (Note: At present, the effect of gravity is ignored and nothing is inferred about the gas–solid or liquid–solid interfacial tensions, or their effect on the contact angle.) The Laplace equation (Eq. (1)) describes the balance for a drop having the shape of a spherical cap with radius r:

$$P_\mathrm{l} - P_\mathrm{g} = \frac{2\gamma_\mathrm{gl}}{r} \tag{1}$$

For a surface of arbitrary curvature $\mathrm{d}A_{ij}/\mathrm{d}V_j$ between bulk phases i and j,

$$P_j - P_i = \gamma_{ij}\frac{\mathrm{d}A_{ij}}{\mathrm{d}V_j} \tag{2}$$

Consequently, the liquid on the concave side experiences a higher pressure P_l than gas on the convex side having pressure P_g.

1.3.1. Liquid (mercury) intrusion porometry

The contact angle of mercury with most pore walls is greater than 90°, which is due to the fact that mercury does not usually wet solid surfaces. When in contact with a porous solid, the gas–liquid surface is concave toward the liquid; hence, the higher pressure is within the liquid. Therefore, in order to force liquid into a pore, mercury intrusion requires overcoming a pressure difference ΔP across the curved surface. The pressure difference across the hemispherical meniscus in a cylindrical pore is dictated by the Laplace equation. With the geometric relationship between pore radius r_p, surface curvature radius r, and contact angle θ as

$$r_\mathrm{p} = r\cos\theta \tag{3}$$

the pressure difference ΔP across the mercury surface becomes

$$P_\mathrm{l} - P_\mathrm{g} = \Delta P = -\frac{2\gamma_\mathrm{gl}}{r_\mathrm{p}}\cos\theta \tag{4}$$

The sample is evacuated before adding liquid mercury, and a negligible Hg vapor pressure is assumed, $P_\mathrm{g} \approx 0$. The expression (4) is the so-called "Washburn equation" and is used to determine pore size from mercury intrusion. Because $\theta > 90°$ (i.e., $\cos\theta < 0$), an excess pressure must be applied to force liquid into the pores. The take-home point is that surface curvature, which is closely related to the pore size, forces a pressure difference that must be overcome for the liquid to fill the pore.

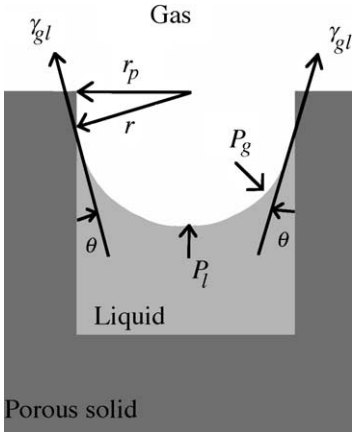

Fig. 1. Sketch of a liquid in a pore at equilibrium with its gas phase. This liquid wets the pore walls with a finite contact angle θ, resulting in a surface curvature r being slightly larger than the pore radius r_p.

1.3.2. Gas (nitrogen) adsorption porometry

In contrast to the mercury intrusion technique, gas adsorption porometry operates on the principle of capillary condensation and necessitates an understanding of the phase transformation from gaseous to liquid nitrogen within a pore. The sketch in Fig. 1 demonstrates a liquid confined in a cylindrical pore in equilibrium with its gas phase wetting the pore wall with a finite contact angle θ. This simple picture corresponds to the high-pressure region of an adsorption isotherm where pore filling is taking place. The low-pressure regime of monolayer adsorption is not considered, and gravitational effects are ignored. The resultant gas–liquid surface tension γ_gl causes hemispherical menisci to form.

For a perfectly wetting fluid (i.e., $\theta = 0$), the radius of curvature r is identical to the pore radius $r_\mathrm{p.}$ The liquid is on the convex side of the interface. Inspection of the Laplace equation shows that the vapor pressure of the gas phase must be greater than the hydrostatic pressure of the liquid if the phases are to coexist at equilibrium. This picture represents the nitrogen adsorption method for determining pore size.

One approach to determining the pore radius uses the Gibbs–Duhem equations to describe the thermodynamic equation of state for coexisting liquid and gas phases (see Appendix A.2 for derivation summary). The Laplace equation is used to describe the mechanical equilibrium of the curved gas–liquid interface having surface tension γ_gl. The

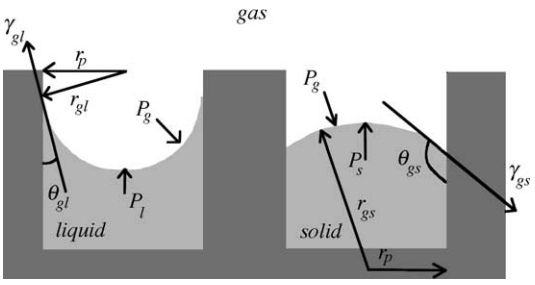

Fig. 2. A porous solid with liquid in one pore, solid in another, each at equilibrium with the gas phase. In this example, the pores have the same radius, but the contact angles θ_{ij}, surface curvature radii r_{ij}, and surface tensions γ_{ij} are different. It is also assumed that the gas–solid interface is concave towards the solid phase.

resulting relationship is known as the Kelvin equation:

$$\ln\left(\frac{P_g}{P_g^0}\right) = -\frac{2\gamma_{gl}v_l}{rRT} \tag{5}$$

It relates the equilibrium vapor pressure P_g of a liquid with specific volume v_l and meniscus radius r to the vapor pressure P_g^0 of the same liquid with a planar surface. Incremental increases of the gas pressure allow capillary condensation to occur in larger pores. Most pore-filling liquids, including nitrogen, have a finite contact angle θ with the pore wall. Recalling the relation between pore radius and contact angle (Eq. (3)) gives a revised Kelvin equation:

$$\ln\left(\frac{P_g}{P_g^0}\right) = -\frac{2\gamma_{gl}v_l}{r_p RT}\cos\theta \tag{6}$$

1.3.3. Thermoporometry

In a thermoporometry experiment, the temperature dependence of the solid–liquid equilibrium is probed at constant ambient pressure, counter to capillary condensation where the pressure-dependent gas–liquid equilibrium is probed at fixed temperature. Defay et al. [7] derived a relationship for the solid–liquid transition temperature T as a function of surface curvature by first considering the triple point of a pure substance. When a closed system contains a single component coexisting in liquid, vapor, and solid forms with planar surfaces, the Gibbs phase rule dictates that the system is invariant, i.e., no thermodynamic degrees of freedom. The triple point can only exist at a single temperature and pressure for a pure substance. However for curved surfaces, the Gibbs phase rule prescribes two independent degrees of freedom. This means two independent curvatures will define the equilibrium between the three bulk phases [7]. Fig. 2 presents a unique situation, whereby a porous material contains coexisting liquid and solid adsorbate in separate pores at a fixed temperature T different from the equilibrium phase transition temperature T_0. This system exhibits a melt/freeze transition temperature shift according to (see Appendix A.2).

$$\ln\left(\frac{T}{T_0}\right) = -\frac{2}{\Delta h_f}\left(\frac{v_l\gamma_{gl}}{r_{gl}} + \frac{v_s\gamma_{gs}}{r_{gs}}\right) \tag{7}$$

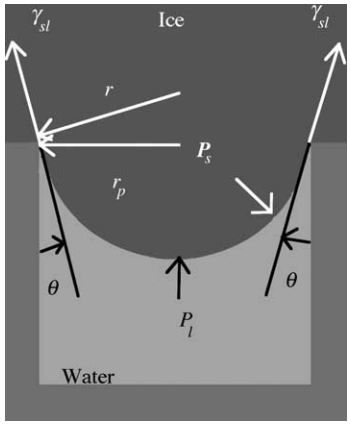

Fig. 3. Typical condition for a thermoporometry experiment where an excess of water has been added to the porous material. At any T below the equilibrium melt temperature T_0, the excess solid phase forms a planar surface with the gas. The pore in this example is small enough (i.e., has a highly curved surface) that only liquid water exists within the pore.

The two surface tensions γ_{ij} and radii r_{ij} are defined in Fig. 2. The specific molar volumes of the solid and liquid phases are v_s and v_l, respectively, and the molar heat of fusion Δh_f has been introduced. When the liquid wets the pore wall and the solid phase does not, the phase-transition temperature for the substance within the pore will always be lower than the same substance outside the pore. Note that the pore radius r_p is, again, related to the menisci curvatures through the contact angles θ_{gl} and θ_{gs}.

In the typical thermoporometry experiment, one uses a liquid that completely wets the pores, thereby filling all accessible voids by capillary action. If an excess of liquid is added, overfilling the pores, the gas–liquid and gas–solid interface is planar above and below the solidification temperature T_0, respectively. Therefore, the gas phase no longer needs to be considered. This situation is depicted in Fig. 3 where water is shown as the pore-filling liquid. For the liquid within the pores, a simpler relationship for the solid–liquid phase transition exists between the bulk transition temperature T_0, the solid–liquid surface curvature r, and ambient temperature T, when the two phases are in equilibrium, as derived in Appendix A.3.

$$\ln\frac{T}{T_0} = -\frac{2v_l\gamma_{sl}}{\Delta h_f r_{sl}} \tag{8}$$

Expansion of the logarithm on the left-hand side gives

$$\ln\frac{T}{T_0} = \ln\left(\frac{T_0 - \Delta T}{T_0}\right) = \ln\left(1 - \frac{\Delta T}{T_0}\right) \cong -\frac{\Delta T}{T_0} \tag{9}$$

The specific molar volume and molar heat of fusion are substituted according to

$$v_l = M/\rho_l \tag{10}$$

$$\Delta h_f = \Delta H_f/M \tag{11}$$

This provides a final relationship between the temperature depression ΔT and the pore radius r_p.

$$\Delta T \cong \frac{2T_0\gamma_{sl}}{\rho_l \Delta H_f}\frac{\cos\theta}{r_p} \quad (12)$$

M is the probe liquid molecular weight, ρ_l the liquid mass density, and the relationship between the solid–liquid surface curvature r, pore radius r_p, and contact angle θ is given in Eq. (3). Eq. (12) is analogous to the Gibbs–Thompson equation, which predicts the melting point depression of small crystalline solids, and includes the reciprocal relationship between the temperature shift and pore radius.

Many studies have noted that a layer of non-freezable liquid usually exists along the walls of a porous material. For example, nominal water layer thicknesses between 0.5 and 2.0 nm in silica hydrogel materials have been reported [19–21], corresponding to several monolayers. The permanent liquid layer of thickness δ effectively decreases the radius of the dispersed solid phase. Thus, for very small pores, the more precise relationship between the temperature shift and pore radius is written

$$\ln\frac{T}{T_0} = -\frac{2\gamma_{sl}}{\rho_l \Delta H_f}\frac{\cos\theta}{(r_p - \delta)} \quad (13)$$

As a final note, there is an implicit assumption that over the temperature interval, T to T_0, the surface tension, density, and heat of fusion are independent of temperature. However, there are instances where large temperature ranges are covered, i.e., very small pores. Empirical expressions for these parameters are usually cited in polynomial form; examples for water as a probe liquid have been cited in the literature [6,9,21].

2. Experimental

2.1. Materials and sample preparation

Water used as the probe liquid was obtained from an in-house distilled water source. The organic solvents cyclohexane, 1,4-dioxane, and chlorobenzene were analytical grade and were used without further treatment. The relevant physical properties of the probe liquids are summarized in Table 1. Controlled-pore glass samples (CPG) were purchased from Electro-Nucleonics Inc., Fairfield, NJ. A summary of the CPG characteristics, as supplied by the manufacturer, measured by mercury intrusion and nitrogen adsorption methods, is given in Table 2. While others [12] advocate surface derivatization to promote wetting by organic liquids, no such treatment was used in this study because the CPG samples were used as received.

The controlled-pore glass samples were moistened with the probe liquid before transferring to pre-weighed aluminum pans. Although no specific studies were conducted on the time dependence of liquid uptake into the porous materials, no systematic differences were observed for the CPG samples measured immediately after preparation versus those left in a moistened state for extended periods. Porous CPG-to-liquid weight ratios were determined by a difference method. The DSC pans were weighed before and after addition and sealing of the wet porous solid. After the measurement, the pans were pierced and heated in a laboratory vacuum oven held at 100–110 °C until constant weight was obtained. The residual weight of the dried pan was taken as the amount of porous solid initially added. The weight loss from drying was taken as the total amount of probe liquid contained in the sample. In addition, for measurements with the more volatile organic solvents, it was important to weigh the hermetic pans before and after the DSC experiments to verify a constant solid-to-liquid ratio.

To test the feasibility of thermoporometry for examining thin coatings of porous particles held by a binder polymer, two hand coatings were prepared. One was prepared from an aqueous solution of approximately 80 wt.% of 37.9 nm diameter CPG and 20% poly(vinyl alcohol) (Gohsenol GH-17 from Nippon Gohsei Co., Japan) because the binder polymer was coated on borax subbed, polyethylene resin-coated (RC) paper. The dried layer thickness was approximately 100 μm. The second coating contained fumed alumina particles (Cab-O-Sperse® PG003, Cabot Corp.) in a poly(vinyl alcohol) binder, which was applied to a corona discharge-treated RC paper base. Paper punches were used to create

Table 1
Physical properties of probe liquids

	T_m^0, K (°C) [24]	ΔH_f (J/g) [24]	ρ_{liquid} (g/cm^3) [24]	ρ_{solid} (g/cm^3)
Water	273.15 (0)	334	1.000[a]	0.917[a]
Cyclohexane	279.75 (6.6)	31.3	0.779[b]	0.833[c]
Chlorobenzene	227.55 (−45.6)	85.4	1.106[b]	1.225[d]
Dioxane	284.95 (11.8)	146	1.034[b]	–

[a] At 273 K.
[b] At 293 K, relative to water at 277 K.
[c] Determined from unit cell dimensions [51].
[d] Determined from unit cell dimensions at 93.15 K [52].

Table 2
Characterization parameters for controlled-pore glass samples

Mean pore diameter (nm)	Pore size distribution (%)	Pore volume[a] (cm^3/g)	Surface area[b] (m^2/g)
208.4	6.1	0.87	8.2
127.3	8.4	1.19	24
101.0	8.5	0.79	21.8
54.7	6.9	1.13	43.1
52.3	3.9	1.13	41
37.9	6.8	1.49	95.0
18.2	4.7	0.97	112.7
12.8	5.1	0.80	141.2
7.5	6.0	0.47	140

[a] As reported by supplier, measured by Hg intrusion.
[b] As reported by supplier, measured by nitrogen adsorption.

3.5 mm diameter paper disks that were placed, coating-side down, in a hermetic DSC pan. Approximately 1–5 mg of water was added, and the excess liquid was removed with a tissue by capillary action. Next, the hermetic pans were sealed and weighed. The actual water weight was determined by the gravimetric difference method mentioned above. A sample of the same fumed alumina suspended in water with a 40 wt.% solid was examined as received for a comparison of the pore size distribution in the second coated paper sample.

Porous and solid organic beads were synthesized in-house. One series of porous beads were a class of styrene and/or acrylate-based copolymers whose syntheses were by suspension and emulsion polymerization methods taken from the literature [22,23]. Other porous beads were polyester-based with monomers having a combination of ionic and non-ionic character. The polyester bead is composed of an aliphatic polyester, divinyl benzene as a cross-linking agent, and chloromethyl styrene quaternized with dimethylethanolamine. Some of the samples were also characterized for porosity and specific surface area by nitrogen adsorption, using a Quantachrome NOVA-3000 Multi-Point Gas Adsorption Analyzer (measurements are courtesy of E. Voll, Eastman Kodak Company). The polymeric beads were received in powdered form. If dried cakes or flakes were present, they were ground with a mortar and pestle. The samples were usually pre-wetted by adding small amounts of liquid (usually water) until a moist paste was formed. Sometimes, light mechanical stirring of the mixture was necessary to achieve complete wetting of the powders. Approximately 3–6 mg of wet powder was placed in the bottom of a hermetic DSC pan and lightly tamped to get good contact with the bottom surface before sealing. The actual liquid and dried polymer particle weights were determined gravimetrically after the thermoporometry experiments as noted above.

2.2. Calorimetry

Calorimetry experiments were performed by using any of several laboratory differential-scanning calorimeters from TA Instruments (model 2920 or model Q1000); each was equipped with a refrigerated cooling unit for controlled cooling and sub-ambient temperature operation. A constant furnace atmosphere was maintained with a house nitrogen purge. Calibration for heat flux and temperature was done with an indium metal standard at the same scan rates as the experiments. For measurements carried out while in the heating mode, a verification of the temperature calibration can be noted from the extrapolated melt onset of the excess solid phase. Even with the large temperature difference between the melt temperature of indium metal (429.75 K (156.6 °C) [24]) and the melting of the excess solidified probe liquid (for example, 273.15 K (0 °C) for water, and 279.75 K (6.6 °C) [24] for cyclohexane), seldom was the temperature offset more than 0.1–0.2 K. This observation assures linearity of the DSC temperature scale. Furthermore, pore radii are determined from the melting-point depression, relative to the excess phase, so the sample, itself, was internally calibrated for temperature.

Small-volume aluminum hermetic pans, supplied by the vendor, were used to encapsulate the samples with a mechanical press. Sample size was observed to affect the shape of the melt peak, particularly the peak caused by the excess phase. In order to keep the melt peaks as narrow as possible, the liquid masses were kept low, on the order of 1–2 mg. The scanning rates were dependent on the probe liquid, and the desired temperature resolution. For example, a very low scan rate of 0.05 K/min was used when water was the probe liquid, and a small temperature depression (e.g., less than 5 K) was expected. This slow rate enabled the resolution of very small temperature shifts for materials with large pores. The large heat of fusion of the melt transition for water negated the effect of low signal-to-noise in the heat flow signals, which were expected because of the slow scanning rate. The scanning rates with other probe liquids are cited within the discussion.

The protocol for the DSC measurement varied from sample to sample, but the general approach is as follows. Supercooling of the probe liquid was a common occurrence, so all samples were quenched to far below the equilibrium freezing temperature. A large exothermic response in the real-time signal indicated that the sample had frozen. Thermoporometry measurements on frozen samples were done either in a heating-only mode through the melt transition of the pore and excess liquid, or by a heat/cool procedure similar to that reported by Ishikiriyama et al. [19]. The latter method involves quenching, slowly heating through the pore melt region until melting of the excess (external) phase just commences, then cooling at the same slow rate through the freezing of the dispersed phase. The pores are open to the exterior; therefore, the presence of the frozen external phase serves to nucleate the crystallization of the confined liquids once the equilibrium transition temperature dictated by the pore size is reached.

3. Results and discussion

3.1. Water in controlled-pore glasses—experimental conditions

3.1.1. Dependence of temperature shift ΔT on scan rate

A review of the literature reveals no general consensus for DSC temperature programs, as experimental conditions are often dictated by many variables: the characteristics of the porous solid, the solidification temperature of pore-filling liquid, the sample size, the instrument capabilities, and most often, the analyst preferences. For example, scan rates from 15 K/min [14] down to 1 K/h [25] have been reported in some of the more detailed thermoporometry studies. Hay and Laity [26] presented a recent study of the effect of heating rate on endothermic and exothermic responses to follow the kinetics of water migration out of porous cellulose membranes. In the present study, it is assumed that the probe liquid does not

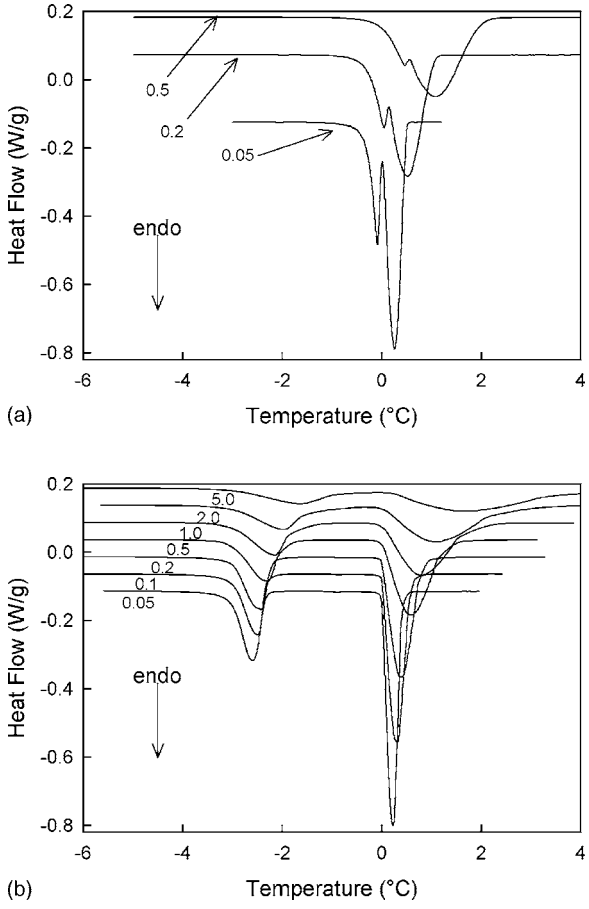

Fig. 4. DSC curves at various heating rates for water in: (a) 208.4 nm and (b) 18.2 nm diameter CPG. The lower temperature endothermic response is due to the melting of the confined water. The scanning rates are shown for each curve with units of K/min. The data have been rescaled to account for the heating rate and shifted along the ordinate to separate the curves.

migrate out of the porous solids, so our focus is to optimize experimental conditions to provide accurate resolution of the dispersed phase and excess melting peaks. Examples of the effect of heating rate are qualitatively displayed in Fig. 4 for 208.4 and 18.2 nm diameter CPG samples having a rigid pore structure. These samples contain an excess of water such that the pore and excess endotherm peaks are present. It is apparent that the 208.4 nm pore sample provides a challenge for the method and underscores that a low scan rate is required to resolve large pores. Even at the lowest rate of 0.05 K/min, it was not possible to obtain baseline resolution of the confined phase. However, the peak separation is sufficient to determine individual peak temperatures as well as the extrapolated onset values. On the other hand, for the 18.2 nm CPG sample, there is peak separation up to a heating rate of 5.0 °C/min, albeit with substantial peak broadening. As with any DSC experiment, there is a trade-off between experimental duration and signal resolution that depends on the pore size.

For a porous material with a narrow pore size distribution, the melting point depression ΔT of the dispersed phase may be determined three ways, as diagrammed in Fig. 5.

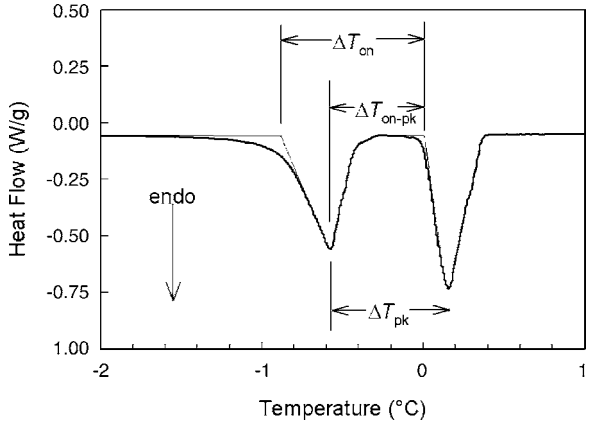

Fig. 5. DSC heating curve for water in 54.7 nm CPG showing the three methods for determining the melting temperature depression ΔT, described in the text as the peak-difference (ΔT_{pk}), onset-difference (ΔT_{on}), and onset–peak ($\Delta T_{on\text{-}pk}$) methods.

The first is by the separation of peak maxima (ΔT_{pk}: "peak-difference" method), the second from the difference between extrapolated onsets (ΔT_{on}: "onset-difference" method), and the third is from the difference between the peak maximum of the pore phase and the extrapolated onset of the excess phase ($\Delta T_{on\text{-}pk}$: "peak-onset" method). The influence of the scan rate on ΔT for two of these methods, ΔT_{pk} and ΔT_{on}, is shown in Fig. 6 for three CPG samples. There is only a slight sensitivity to the heating rate for the smaller pore, 12.8 and 54.7 nm CPG samples. Additionally, the temperature shift depends on the calculation method, with ΔT_{pk} slightly smaller than ΔT_{on}. The latter observation is not unexpected because the pore size distributions, though quite narrow as shown in Table 2, are not identical for the various CPG materials. The largest pore, 208.4 nm diameter sample exhibits a dramatic dependence both in the scan rate dependence and in the lack of agreement of ΔT by the two methods. Note, however, that the results nearly coincide upon extrapolation to a null heating

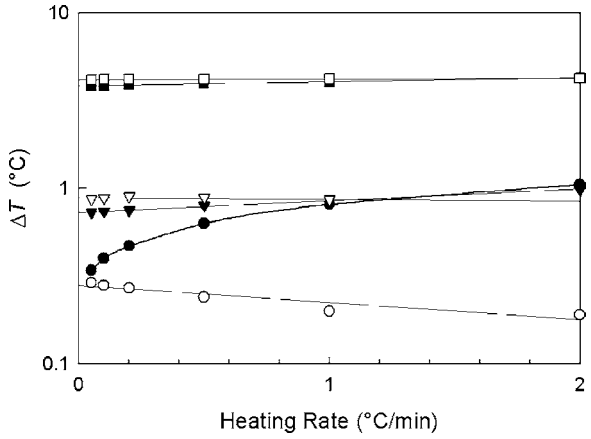

Fig. 6. Melting point depression ΔT (log scale) as a function of heating rate for three CPG samples: pore diameters 12.8 nm (□, ■), 54.7 nm (▽, ▼), and 204.6 nm (○, ●) by the peak-difference (filled) and onset-difference (open) methods.

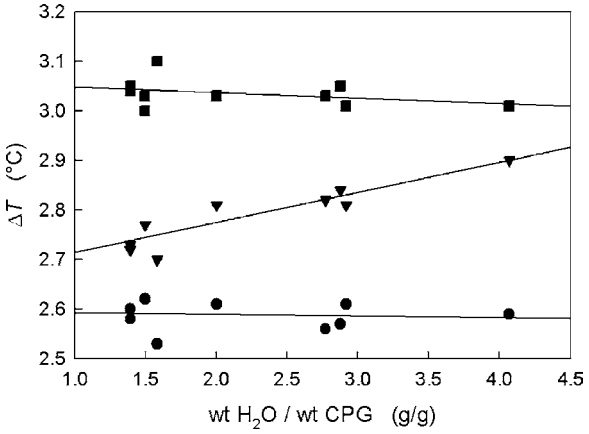

Fig. 7. Melting point depression ΔT for 18.2 nm CPG from DSC heating scans at 0.05 K/min as a function of the water-to-CPG ratio. The symbols are for ΔT_{pk} (▼), ΔT_{on} (■), and $\Delta T_{on\text{-}pk}$ (●) methods.

rate. The ordinate is displayed on a logarithmic scale to emphasize the scan-rate dependence for the large pore, 208.4 nm CPG sample.

3.1.2. Liquid-to-porous solid ratio

Another variable that has seen some attention in the literature is the liquid-to-porous solid mass ratio both above and below the saturation point. Ishikiriyama and Todoki [9] followed the trend of pore- and bulk-melt endotherm areas to determine the amount of freezable and non-freezable water as a function of water-to-silica ratio. No comments concerning the effect on ΔT were mentioned. Jackson and McKenna [12] note a decrease in the mass-normalized endotherm area, i.e., ΔH_f, for incompletely filled pores containing *cis*-decalin and benzene. This leads to a variation in the melting point depression of about ±1 K, as measured by ΔT_{pk}; no trend with liquid-to-porous solid ratio were reported, though an increase in the precision of ΔT_{pk} was noted for completely filled pores. Rennie and Clifford [8] comment that the melting temperature of water within the pores of CPG varies for unsaturated samples but becomes constant upon reaching the filled pore limit. For the purpose of an accurate correlation of pore size to melting point depression ΔT, none of these studies explicitly examined the effect of the liquid-to-porous solid mass ratio. Small pores produce a large temperature depression; hence, the relative effect is likely to be minimal. However there may be concern with large pore samples, where an uncertainty in ΔT of even a few tenths of a degree K will lead to a large uncertainty in pore size.

To highlight this point, the data in Fig. 7 are for 18.2 nm CPG with varying water-to-CPG mass ratios; all samples are saturated with water, making the pore and excess melt endotherms visible. The total sample mass was kept in the range of 4–7 mg with a heating rate of 0.05 K/min to minimize thermal lag. As the water-to-CPG ratio increases, the area and width of the excess-phase endotherm increases, while the width of the pore melt peak remains constant, indicating that the breadth of the latter is more reflective of the pore size distribution rather than thermal lag. The net effect is that the apex of the excess water melt peak gradually moves to higher temperatures, causing the peak difference ΔT_{pk} to increase with the water-to-CPG ratio. However, the extrapolated onset temperatures for both the pore and excess melts are largely unaffected by the amount of water, and the pore melt apex position does not vary either. Similar observations have been recorded for samples of 37.9 and 101.0 nm CPG not shown here. In order to measure the melting point depression with little dependence on the water-to-CPG content, either the onset–peak ($\Delta T_{on\text{-}pk}$) or the onset-onset (ΔT_{on}) difference methods seem equally appropriate. This observation suggests that the peak-difference method used in many studies may have lead to errors if consistent liquid-to-porous solid mass ratios were not used. It is noted that Titulaer et al. [25] determine temperature shift with the onset–peak difference method. The CPG pore dimensions given in Table 2 represent the peak value of a size distribution; therefore, the (excess) onset − (pore) peak difference $\Delta T_{on\text{-}pk}$ approach is more appropriate and therefore is recommended for calibration.

3.1.3. Heating versus cooling experiments

Up to this point, the discussion has focused on melting experiments only. Before continuing to the cooling experiments, a few clarifying comments are in order. The terms *supercooling* and *undercooling* are sometimes used to describe the delayed onset of liquid-solidification. In the context of this discussion, *supercooling* refers to the metastable liquid state of a liquid below its equilibrium freezing temperature, absent of the porosity effect. The metastability occurs because solidification is a nucleation-driven process whereby a critical nucleus size is required for crystal growth. In a pure, homogeneous fluid, spontaneous density fluctuations increase in size with decreasing temperature, only to reach the critical nucleation size at a sufficiently low temperature. The freezing (crystallization) temperature for a supercooled liquid is usually not reproducible with any precision. Conversely, *undercooling* denotes the presence of liquid below the equilibrium freezing temperature solely because of its confinement within the pores. The freezing temperature of an undercooled liquid inside a pore is reproducible, so long as the excess phase at the pore opening is solid. Therefore supercooling is to be avoided, and freezing of the undercooled liquid is what is measured. Others [6,19,27–29] have observed supercooling of water in porous media, but we avoid it here.

An experimental melt/freeze protocol is demonstrated in Fig. 8 for water in 37.9 nm pore diameter CPG. The lower curve in the figure is for a frozen sample that is heated until it has fully melted and shows complete separation of the pore and excess ice endotherm transitions. If one were to cool the sample slowly from above the equilibrium melting point (for example, starting at 274 K (i.e., 1 °C)), neither the excess nor the pore water freezes until significant supercooling has occurred—at which point the entire liquid phase spontaneously freezes. The instability of supercooled water is such that a marked exothermic response is typically ob-

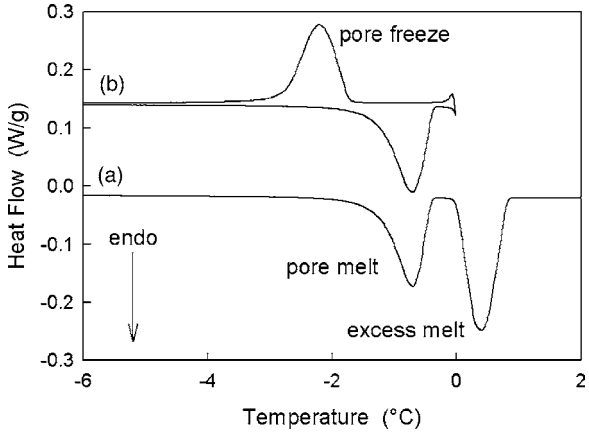

Fig. 8. (a) DSC heating curve for 37.9 nm diameter CPG saturated with water. The sample was frozen by rapidly quenching to −25 °C. (b) Heating/cooling curve showing a melt/freeze hysteresis. The scanning rate for both curves is 0.05 K/min.

served upon rapid crystallization in an approximate interval of −15 to −20 K below the expected pore freezing temperature. The upper curve of Fig. 8 is recorded by first quenching the sample as before, heating until just before the excess ice phase melts, followed by an immediately switch to cooling. At this moment there is liquid water in the pores and solid ice outside. Upon cooling, the bulk ice phase serves to nucleate crystallization at the pore openings when the appropriate transition temperature, dictated by the pore size, is reached.

The slow scanning rate adopted for the experiments on the model CPG materials is required to enable the resolution of minute temperature depressions from the bulk transition, an important matter with large pore dimensions. It also follows that the narrow size distributions of CPG, with a fairly sharp cut-off at the upper end of the distribution, provides a good test for the capability of the method. A clear demonstration of the resolving power of thermoporometry is shown in Fig. 9 where a mixture of seven controlled-pore glasses is examined whose pore diameters range from 208.4 to 7.5 nm. Each individual pore melt and freezing peak is evident in the heating and cooling curves, respectively. Brun et al. [6] present an example of thermoporometry by DSC to distinguish individual pore sizes with data for a binary mixture of a porous glass, although the individual pores were poorly resolved. Similarly, Strange et al. [30] examined a mixture of three porous silicas by NMR spin–spin relaxation experiments. To our knowledge, no demonstration of the resolving power of differential scanning calorimetry for such a complex mixture has been reported.

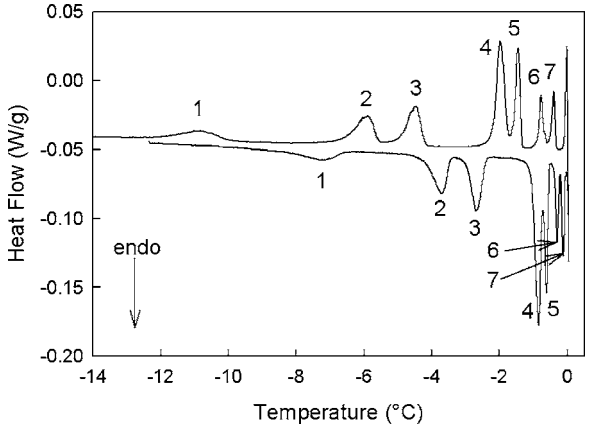

Fig. 9. DSC curves for a melt-freeze experiment of a mixture of seven controlled-pore glasses saturated with water. The peaks labelled 1–7 are for CPGs with pore diameters of 7.5, 12.8, 18.2, 37.9, 52.3, 101.0, and 208.4 nm, respectively.

The larger temperature depression upon solidification, seen in Fig. 9, is the recognized melt/freeze hysteresis phenomenon that has been observed by differential scanning calorimetry [6,10,18–20,27,29,31,32], ac calorimetry [33], specific heat measurements [34], and by techniques not traditionally associated with thermal analysis, such as dielectric spectroscopy [13,35], positron annihilation [36], small-angle neutron scattering [37], dilatometry [38], and various NMR methods [39,40]. The hysteresis has been most commonly interpreted in terms of pore shape and geometry; for example, a simple model of a cylindrical pore predicts that the temperature depression upon melting is half that of freezing, whereas a purely spherical pore will exhibit no hysteresis [6]. A related explanation that takes into account the shape of pores put forth by Enüstün et al. [41] is that melting is controlled by the radius of the pore, and freezing is controlled by the radius of the opening to the pore cavity. This idea has some viability if pore freezing only occurs upon nucleation by an advancing solid phase during cooling; for example, with large bottleneck-shaped pores or interconnected spherical pores. A recent phenomenological free energy model of a cylindrical pore proposed by Denoyel and Pellenq [42] reasons that the interaction between liquid/solid phase and liquid/pore wall interfaces, mediated through interfacial tensions, produces a thermodynamic metastability. The conclusion is that the melt temperature is greater than the equilibrium freezing temperature. Whichever picture is most appropriate, logic dictates that it is important to probe porous materials by both melting and freezing thermoporometry.

From the DSC experiment on the mixed CPG sample from Fig. 9, one is able to construct a "calibration" plot of $\Delta T_{\text{on-pk}}$ versus $1/r_{\text{p}}$, as shown by the open symbols in Fig. 10. The melt/freeze hysteresis is manifested by different slopes obtained upon heating and cooling. These results are indistinguishable from separate experiments on each of the individual samples in Table 2. To confirm this statement, the solid curves in Fig. 10 retrace empirical fits from the latter experiments. The reciprocal relationship between the pore radius and temperature depression stated in the Gibbs–Thompson equation is generally followed. However, there is a subtle non-linearity in the melting point data that hints of a departure from the simplified expression in Eq. (12). Hansen et al. [21] also show a non-linear dependence of ΔT on $1/r_{\text{p}}$, although the range of temperature depression is up to 70 K, much larger than the greatest shift in this study, ca. 10 K. The overall trend

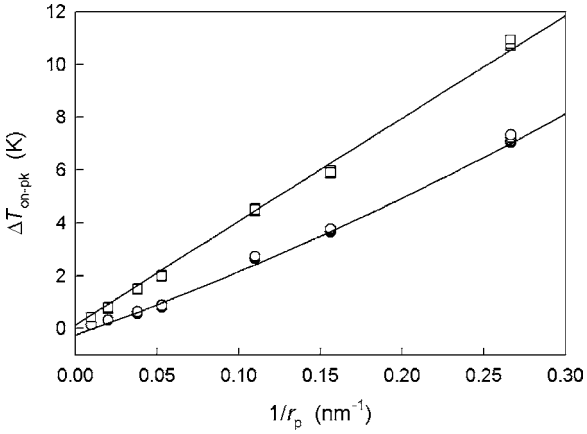

Fig. 10. Melting (circles) and freezing (squares) point depression $\Delta T_{on\text{-}pk}$ vs. reciprocal pore radius r_p on the seven-component CPG mixture. The lines represent second-order linear regression fits to a separate experimental series on nine individual CPG samples.

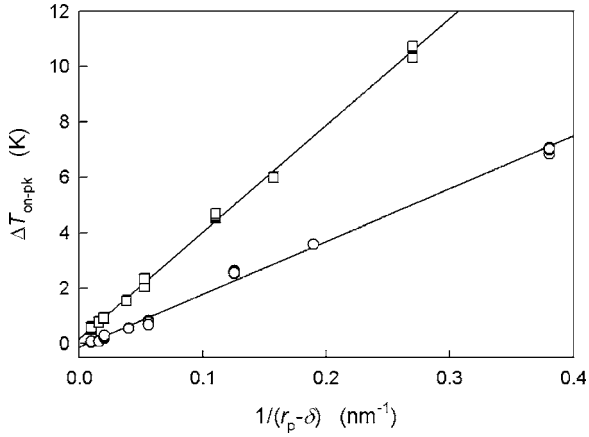

Fig. 11. Melting (circles) and freezing (squares) point depression data for water imbibed in individual CPG samples, plotted against $1/(r_p - \delta)$. The solid lines represent fits to the data with a non-freezable layer thickness $\delta = 1.06$ and 0.04 nm for melting and freezing, respectively.

for most thermoporometry experiments cited in the literature [8,9,12–18] is that of a linear dependence between ΔT and $1/r_p$.

Several possible reasons could explain the non-linearity between $\Delta T_{on\text{-}pk}$ and $1/r_p$. The option of using $\Delta T_{on\text{-}pk}$ to measure the temperature depression, instead of ΔT_{on} or ΔT_{pk}, does not appear to be the cause, as a similar tendency is seen with these other choices. It is also recognized that the Gibbs–Thompson relationship in Eq. (12) is an approximated form of the more exact Kelvin equation, whereby $-\Delta T/T_0$ is substituted for $\ln(T/T_0)$ in the limit of small T/T_0. This change amounts to less than a 2% deviation between Eqs. (8) and (12), when $\Delta T = 10$ K, and $T_0 = 273.15$ K for water. The effect of temperature on the physical quantities ΔH_f, γ_{sl} and ρ_l has been ignored and clearly needs to be considered [19,21]. These dependencies are addressed later when discussing the evaluation of pore size distribution. Finally, the presence of a thin layer of thickness δ of non-freezable liquid adjacent to the pore wall [6] leads to a correction in the Gibbs–Thompson relation such that ΔT is more correctly related to $1/(r_p - \delta)$. This effect has been noted in the experimental observations of Morishige and Kawano [10] and Schreiber et al. [29].

An empirical examination of our data taking into account the premise of a non-freezable layer produces the plots in Fig. 11. The melting data gives a linear fit with $\delta_m = 1.12 \pm 0.10$ nm; interestingly, the freezing branch yields a value of $\delta_f = 0.04 \pm 0.09$ nm, effectively equal to 0 within the uncertainty of the fit regression. As plotted in Fig. 11, linear regression fits to the data provide the following expressions for the melting and freezing temperature shifts, respectively.

$$\Delta T_{on\text{-}pk} = -\frac{19.082}{r_p - 1.12} - 0.1207 \quad \text{(melting)} \tag{14}$$

$$\Delta T_{on\text{-}pk} = -\frac{38.558}{r_p - 0.04} + 0.1719 \quad \text{(freezing)} \tag{15}$$

Note that, as written, the values of ΔT are negative, reflecting that the pore transition temperatures are lower than the bulk value. The revised analysis of Fig. 11, in essence, serves to correlate a length scale with temperature. Strict adherence to the Gibbs–Thompson equation leads to an expected zero intercept. However, the CPG samples with the largest pore sizes have very small temperature depressions such that the pore melting and freezing peaks are not entirely resolved at the baseline. This feature likely promotes a systematic offset that results in the non-zero intercept. Conversely, incorporating δ into the regression influences the fit for the smallest pores, hence at the higher ΔT values. The melting point depression for the smallest pore radius (3.75 nm) is certainly affected by the non-freezable layer. An algebraic manipulation of Eqs. (14) and (15) yields the following "calibration" equations for heating and cooling experiments, respectively. The importance of these expressions will be discussed shortly.

$$r_p\,(\text{nm}) = -\frac{19.082}{\Delta T + 0.1207} + \delta_m \quad \text{(melting)} \tag{16}$$

$$r_p\,(\text{nm}) = -\frac{38.558}{\Delta T - 0.1719} + \delta_f \quad \text{(freezing)} \tag{17}$$

with $\delta_m = 1.12$ nm and $\delta_f = 0.04$ nm for water in CPG.

In the influential paper by Brun et al. [6], expressions were given for the melting and freezing of water in a hypothetical cylindrical pore.

$$r_p\,(\text{nm}) = -\frac{32.33}{\Delta T\,(\text{K})} + 0.68 \quad \text{(melting)} \tag{18}$$

$$r_p\,(\text{nm}) = -\frac{64.67}{\Delta T\,(\text{K})} + 0.57 \quad \text{(freezing)} \tag{19}$$

These equations were not obtained by the same manner as in this study, that is, by measuring ΔT as a function of r_p. Rather, they were found by factoring the experimental temperature dependence of specific heat capacity, heat of fusion, specific volume, and interfacial tension into the Kelvin equation (Eq.

(8)). A more appropriate comparison to this work should be provided from the study of Ishikiriyama et al. [19,20] with the following relations for water in silica gels

$$r_p\,(\text{nm}) = -\frac{33.30}{\Delta T\,(\text{K})} + 0.32 + \delta_m \tag{20}$$

$$r_p\,(\text{nm}) = -\frac{56.36}{\Delta T\,(\text{K})} + 0.90 + \delta_f \tag{21}$$

These expressions were determined with a sophisticated optimization algorithm to best match a complete pore size distribution between thermoporometry and nitrogen adsorption measurements. The parameters δ_m and δ_f were found into fall in the ranges of 0.5 nm$< \delta_m <$ 2.2 nm and 0.6 nm$< \delta_f <$ 2.8 nm [20]. The temperature dependences of ΔH_f, ρ_l, and γ_{sl} were also input as part of the fitting procedure, though with different empirical forms than utilized by Brun et al. [6].

It is not entirely clear why the results from this work in Eqs. (16) and (17) for controlled-pore glass are in conflict with those of (20) and (21) for silica gels. One notable difference between the two studies is the range of pore radii in the porous samples. Ishikiriyama et al. [19] employed samples with radii between 1.8 and 7.5 nm (with corresponding temperature shifts of $-4\,\text{K} > \Delta T > -20\,\text{K}$ upon melting). They have explicitly noted that samples having pore radii *greater* than 10 nm, i.e., with ΔT less than 4 K, deviated substantially from their Eq. (20), and were not used to fit their melting data. The present study covers significantly larger pore sizes with radii from 3.75 to 104.2 nm, hence a much smaller temperature depression range than in the silica gel study [19]. A comparison is given later in this report of the use of the calibration equations to generate pore size distributions of the CPG samples.

3.2. Other liquids in controlled-pore glass

The thermoporometry experiments of Jackson and McKenna [12] demonstrate that organic liquids are also suitable for the filling of porous silica. Mu and Malhorta [14] report the use of cyclohexane in porous silica, and Baba et al. [16] describe the use of *n*-heptane in silica gels. For this study, cyclohexane, chlorobenzene, and 1,4-dioxane were tested; their physical properties are listed in Table 1. These liquids were chosen for the primary reason that their equilibrium solidification temperatures are practically accessible with a laboratory DSC instrument. They are also of interest because of their varying degrees of polarity and hydrophobicity, although these factors are not an explicitly defined variable in this study. For example, chlorobenzene is hydrophobic and polar, cyclohexane is hydrophobic and non-polar, and 1,4-dioxane is hydrophilic and non-polar. Each liquid should present different interactions with the surface of the porous glass samples.

Cyclohexane is a convenient organic liquid because its fusion temperature is 279.7 K (6.6 °C), very close to water. Fig. 12 shows the results of a heating experiment with cyclohexane in the seven-component CPG mixture, employing scan rates of 0.05 and 1.0 K/min. The abscissa in the two plots has been expanded to only show the melting endotherms for the four largest pore radii in the mixture and the bulk phase melt transition (off-scale). As a probe liquid, cyclohexane provides a complete baseline resolution at the 0.05 K/min scanning rate for all pore sizes, even with the largest 208.4 nm diameter sample. A clean separation of each melting peak is still achieved with cyclohexane for a 1.0 K/min scanning rate, improving the measurement cycle time by a factor of 20. The signal-to-noise for cyclohexane is substantially poorer at the slow scanning rates owing to the low heat of fusion relative to water, roughly an order of magnitude less (see Table 1). This condition is improved with the higher scanning rate. Finally, it is also observed that the melting point depression measured by $\Delta T_{\text{on-pk}}$ is unchanged as a function of scanning rate, regardless of pore size. This is in contrast to what was seen for water in 204.6 nm CPG in Fig. 6. This effect is likely related to the reduced thermal lag, which is due to the lower heat of melting and the associated improved peak resolution.

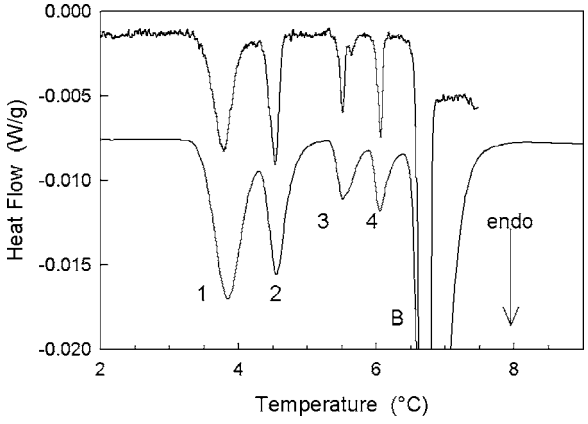

Fig. 12. DSC heating curves for cyclohexane in a mixed CPG sample. The scanning rates are 0.05 and 1.0 K/min for the upper and lower curves, respectively. Peaks 1–4 are for 37.9, 52.3, 101.0, and 208.4 nm diameter pores, and peak B represents the bulk melt transition.

Heating and cooling profiles at 0.05 K/min for chlorobenzene as a probe liquid in the mixed CPG sample is shown in Fig. 13. Some of the individual pore melt peaks are not well separated during the heating step as with cyclohexane; note the poor resolution between the 52.3 and 37.9 nm diameter pore melt peaks. Another significant observation for chlorobenzene is the shifting of the pore melt peak during heat/cool/heat experiments, but only for the larger diameter pores. Examples for the 208.4, 101.0, and 12.8 nm CPG samples are given in Fig. 14. The protocol in these experiments is to solidify the samples with rapid cooling, then a slow first heat through the pore melt transition, slowly cool again to solidify, and finally a slow second heat. For the two larger pore samples, there appears to be a migration of chlorobenzene into smaller pores during the slow cooling step, as indicated by the greater melting point de-

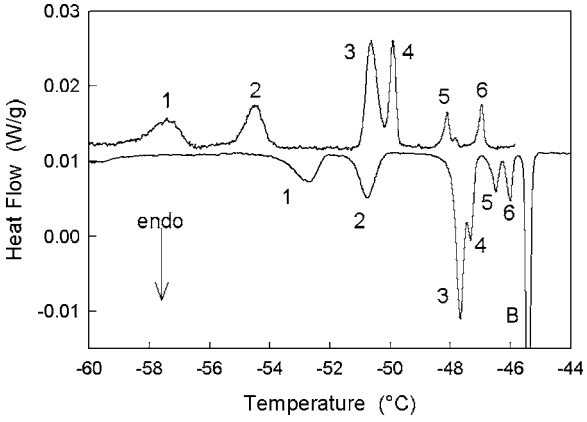

Fig. 13. Heating and cooling curves at 0.05 K/min for chlorobenzene in mixed CPG. Peaks 1–6 are for 12.8, 18.2, 37.9, 52.3, 101.0, and 208.4 nm diameter samples, respectively.

pression the second heat step. No similar peak shift is seen with the smaller pores. If one uses chlorobenzene as a probe liquid, the possibility of liquid migration should be recognized.

A DSC heat/cool profile for 1,4-dioxane in the mixed CPG sample is given in Fig. 15. It was assumed that dioxane could be a convenient and complementary liquid with respect to water and cyclohexane because of its melt temperature of 284.95 K (11.8 °C). Moreover, the etheric groups in dioxane imply a possible H-bonding interaction with the silanol groups in the porous silica, analogous to water. Apart from the pore melt (and freezing) peaks, a large spurious transition near 0 °C in Fig. 15, as well as small side peaks on some of the pore melt transitions, also appear. The transition at 0 °C is assumed to be from the melting of ice, which has appeared to contaminate the sample. The difficulty encountered with 1,4-dioxane is its hygroscopic nature, indeed, its complete miscibility with water [24]. Repeated trials with fresh dioxane and thoroughly dried CPG samples were not entirely successful in eliminating the water interferences. Other experiments, not shown here, seem to demonstrate that the porous glass is able to partition water into pores separate from the dioxane, as supported by the presence of individual pore-water melt peaks in samples that have been allowed to let stand.

The results for the melting and freezing point depressions, $\Delta T_{\text{on-pk}}$, for cyclohexane, chlorobenzene, 1,4-dioxane, and water as a function of the reciprocal adjusted pore radius $1/(r_p - \delta_i)$ are displayed in Fig. 16. The parameters from least-squares regression fits to the general expression in Eq. (22) for both heating and cooling experiments are given in Table 3.

$$\Delta T_{\text{on-pk}} = \frac{A_i}{r_p - \delta_i} + B_i \tag{22}$$

where the subscript i = m or f for melting and freezing, respectively. The melt/freeze hysteresis is present for all of the hydrocarbon liquids. Each liquid exhibits a larger depression of the phase transitions compared to water, and the ratio of the freezing and melting slopes, A_f/A_m, is approximately 2, with the exception of 1,4-dioxane with a ratio closer to 1.5. Because A_i is a function of ΔH_f, ρ_l, γ_{sl}, and liquid/pore wall interactions through the contact angle term $\cos\theta$ (cf. Eq. (12)), the numerical differences between the respective A_i are not unexpected.

There may be an advantage to using hydrocarbon liquids for thermoporometry characterization of large-pore materials because of the larger temperature depression versus water. For example, at a scan rate of 0.05 K/min, the value for $\Delta T_{\text{on-pk}}$ of 0.10 K is easily measured. According to Eq. (22) and the parameters in Table 3, the pore diameter with water as a probe liquid and $\Delta T_{\text{on-pk}} = 0.10$ K is 175 nm. The same temperature depression would translate to a pore diameter of 720 nm for chlorobenzene and 950 nm for cyclohexane. On the other hand, hydrocarbon liquids tend

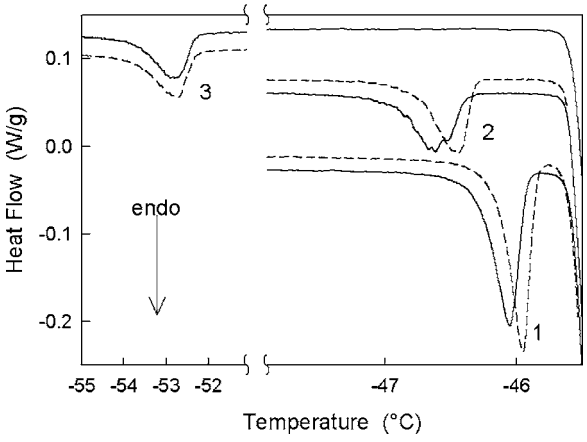

Fig. 14. Melting curves for chlorobenzene in: (1) 208.4 nm CPG, (2) 101.0 nm CPG, and (3) 12.8 nm CPG. The dashed curves represent the first heat scan of the rapidly solidified sample, and the solid curves are for a second heat scan after a slow cooling step. The curves have been shifted for clarity. All measurements are at 0.05 K/min.

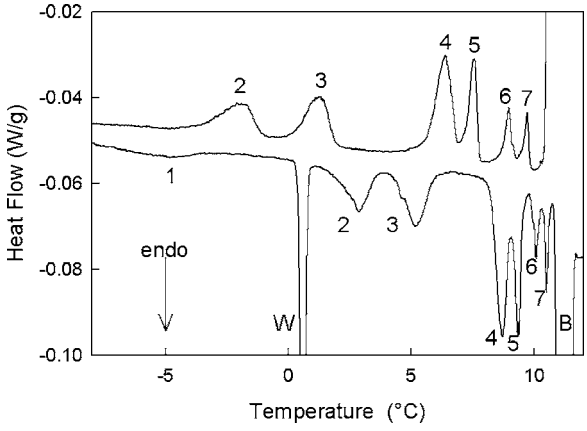

Fig. 15. Heating and cooling curves at 0.05 K/min for 1,4-dioxane in mixed CPG. Peaks 1–7 are for 7.5, 12.8, 18.2, 37.9, 52.3, 101.0, and 208.4 nm diameter samples, respectively. An additional strong endothermic peak seen near 0 °C is attributed to the melting of water that is partitioned into pores separately from the dioxane.

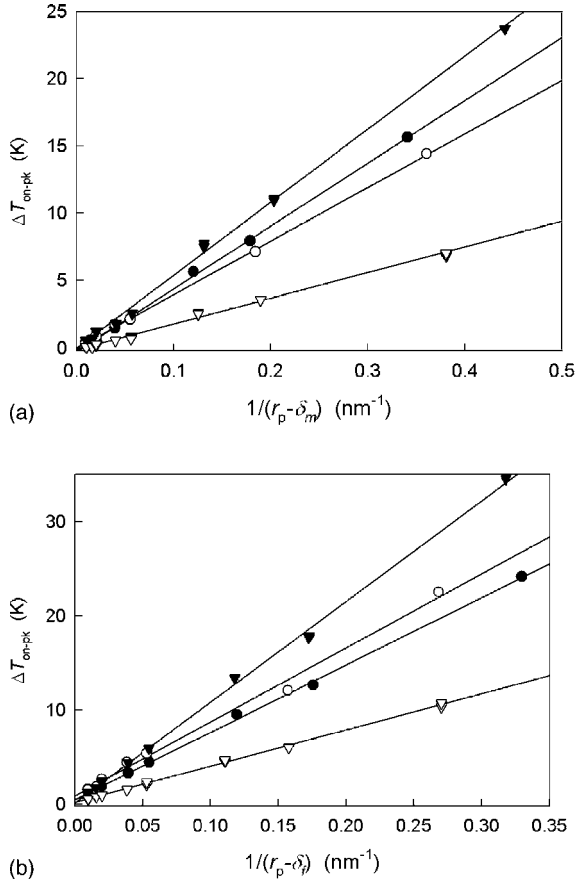

Fig. 16. The results for the (a) melting point depression, and (b) freezing point depression $\Delta T_{on\text{-}pk}$ vs. the reciprocal adjusted pore radius $1/(r_p - \delta_i)$ for cyclohexane (▼), chlorobenzene (◯), 1,4-dioxane (●), and water (▽).

to be somewhat more difficult to handle because of their volatility under ambient laboratory conditions. Solvent loss during sample preparation is often experienced. Moreover, while rigid porous materials such as silica-based glasses may be suitable for analysis, the definite possibility of swelling or dissolution of porous organic materials should be considered.

3.3. Pore volume measurement

Total pore volume V_p (e.g., cm^3 pore per gram porous solid) is another important parameter for characterizing porous materials. A simple calculation of V_p can be obtained

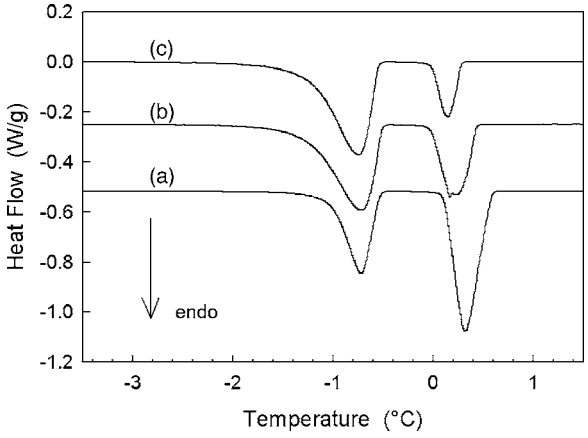

Fig. 17. DSC heat flow profiles for cyclohexane in 37.9 nm diameter CPG at c_{liq}/c_{cpg} of (a) 2.70 g/g, (b) 2.52 g/g, and (c) 1.26 g/g. The area of the pore melt endotherm increases relative to the excess melt peak with decreasing c_{liq}/c_{cpg}.

from a single thermoporometry heating experiment using

$$V_p = \frac{\Delta H_{pore}}{\Delta H_{tot}} \frac{c_{liq}}{c_{solid}} \frac{1}{\rho_{liq}} \tag{23}$$

where a known mass of liquid c_{liq}, of density ρ_{liq}, is added to a known mass of porous solid c_{solid}. The pore melt area, ΔH_{pore}, and combined pore and excess melt peak areas, ΔH_{total}, are determined from the DSC melt endotherms, and their ratio is related to the fraction of liquid contained in the pores. The expression assumes a temperature-independent heat of fusion ΔH and liquid density, as well as a sufficient separation of the pore and excess melt peaks to independently integrate their areas. It is also assumed that all of the liquid has frozen during the initial quench cooling step and melts during heating, i.e., the contribution of the thin liquid layer adjacent to pore walls, and other non-frozen liquid, is negligible.

In the typical thermoporometry experiment, the porous solid is saturated with the probe liquid, and two melting transitions are observed upon heating: the pore melt and the excess phase melt. As one decreases the amount of liquid relative to the solid, the area of the excess peak decreases relative to the pore peak. Examples of the changing peak areas for the 37.9 nm diameter CPG are given in Fig. 17 for cyclohexane. Similar observations are observed with the other probe liquids. It stands to reason that, if one were to

Table 3
Non-linear least-squares fit parameters to Eq. (22)

	Melting			Freezing			
	A_m	B_m (K)	δ_m (nm)	A_f	B_f (K)	δ_f (nm)	A_f/A_m
Water[a]	19.082	−0.1207	1.12	38.558	0.1719	0.04	2.02
Cyclohexane[a]	54.265	−0.0144	1.48	106.92	0.1493	0.60	1.97
Chlorobenzene[a]	39.790	0.0109	0.98	78.694	0.8757	0.02	1.98
1,4-Dioxane[b]	46.638	−0.2469	0.82	71.690	0.4794	0.72	1.54

[a] Scan rate = 0.05 K/min.
[b] Scan rate = 0.1 K/min.

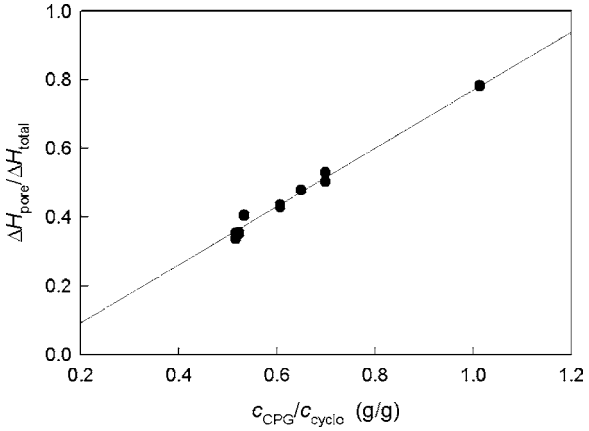

Fig. 18. A systematic change of 18.2 nm diameter CPG to cyclohexane mass ratio provides a quantitative measure of the total pore volume V_p from the slope and the liquid density. The thermoporometry value, 1.11 cm^3/g, compares favorably with the stated Hg intrusion value of 0.97 cm^3/g, cf. Table 2.

continue reducing the liquid level to the point where the only intraparticle pores are filled by capillary action, only the pore melt peak would be present. Extrapolation of a liquid-to-CPG concentration series, thus, leads to a quantitative measure of the total pore volume. One representation of such analysis is shown in Fig. 18 with a plot of $\Delta H_{pore}/\Delta H_{total}$ versus (c_{solid}/c_{liq}). A simple rearrangement of Eq. (23) shows that the slope of such a plot provides $V_p\rho_{liq}$. For this example, $V_p = 1.11\,cm^3/g$ for 18.2 nm CPG with *cyclohexane* as the pore liquid, which compares favorably with the stated Hg intrusion value of 0.97 cm^3/g (see Table 2). Another example using a different extrapolation procedure, $\Delta H_{excess}/\Delta H_{pore}$, as a function of c_{liq}/c_{solid}, is provided in Fig. 19 for *water* in 101.0 nm diameter CPG. In this instance, the *x*-intercept is $V_p\rho_{liq}$, giving the total pore volume V_p as 0.69 cm^3/g, compared to 0.79 cm^3/g from Hg intrusion.

An overall assessment of extrapolation methods and single thermoporometry scans according to Eq. (23) is shown in

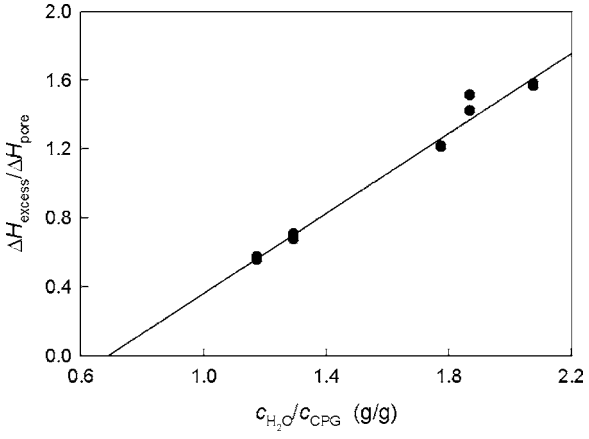

Fig. 19. A concentration series for water in 101.0 nm CPG. The ratio of the excess melt and pore melt areas, when extrapolated to the *x*-intercept, directly provides the total pore volume V_p as 0.69 cm^3/g, compared to 0.79 cm^3/g from Hg intrusion.

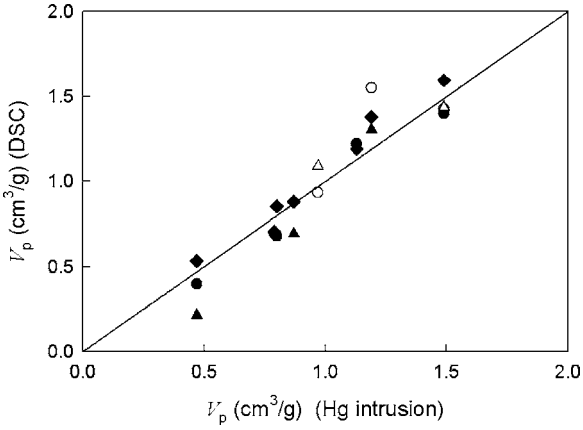

Fig. 20. A correlation plot of total pore volume V_p for the CPG samples in Table 2 as determined by thermoporometry and Hg intrusion. The solid line represents one-to-one correspondence and is not a linear fit to the data. Open symbols are from extrapolation analyses, and solid symbols are for single DSC experiments analyzed according to Eq. (23). The probe liquids are water (○, ●), cyclohexane (△, ▲), and chlorobenzene (◆).

Fig. 20 where the total pore volume is compared to the Hg intrusion values from Table 2 for each of the CPG samples. Included in this plot are results for water, cyclohexane, and chlorobenzene as the probe liquids, where the liquid densities were used to establish the pore volume.

3.4. Pore size distribution

The importance of having a quantitative description of a porous solid via its pore size distribution resides not only in the fact that important physical parameters, such as mean pore size, total pore volume, and specific surface area can be calculated, but also, the shape of the distribution provides an additional perspective. A thorough experimental treatise on pore size distribution (PSD) derived from thermoporometry data has been presented by Ishikiriyama et al. The discussion that follows uses some of the same transformation steps to convert a DSC heating or cooling profile into a differential pore volume versus pore radius plot, i.e., a pore size distribution. Exceptions and deviations to the procedures cited by Ishikiriyama et al. [19,20] are noted.

To transform a DSC profile into a size distribution, the temperature record is converted into an equivalent length scale (for example, pore radius) and the heat flow output from the melting or solidification into a differential pore volume. The groundwork for each of these steps has been established in the preceding sections of this report. The theoretical basis for relating temperature to pore radius is through the Gibbs–Thompson equation (Eq. (12)), but for the purpose of this work, the empirical relationship summarized in Eq. (22) is employed with the solvent-specific parameters listed in Table 3. The pore size is related to the temperature depression ΔT rather than the absolute temperature T; therefore, the onset temperature for the bulk phase melt must be subtracted from the temperature axis of the DSC profile. The

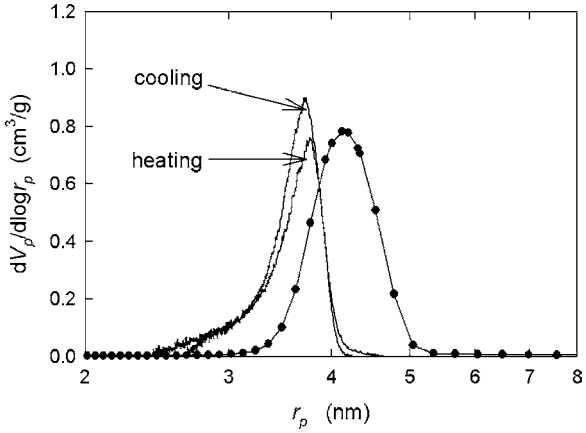

Fig. 21. Pore size distribution for 7.5 nm diameter CPG determined by thermoporometry (solid lines) with water as the pore-filling liquid and Hg intrusion (line with filled points). The Hg intrusion data are not plotted to scale with respect to the ordinate. DSC scan rate = 0.05 K/min.

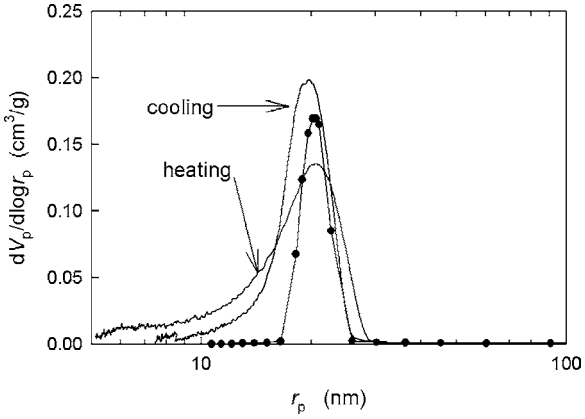

Fig. 22. Pore size distribution for 37.9 nm diameter CPG and water determined by thermoporometry (solid lines) and Hg intrusion (line with filled points). The Hg intrusion data are not plotted to scale with respect to the ordinate. DSC scan rate = 0.05 K/min.

result is a rescaled temperature axis ΔT that can be directly transformed into pore radius r_p. For example with water as the probe liquid, one would use Eq. (16) for a heating experiment, or Eq. (17) for a cooling experiment. It is assumed that the onset of freezing of the bulk phase is the same as the onset temperature for melting.

The second step in the transformation is somewhat more elaborate, although not exceedingly difficult to follow. The heat flowing into a saturated sample upon melting, or out of it on freezing, gives a measure of the amount of the pore liquid undergoing the phase transition. In the previous section, the integrated heat-flow signal was used to calculate total pore volume through Eq. (23). To determine the differential pore volume dV_p/dr_p, the latent heat of fusion (or crystallization) has to be determined at each temperature. This requires a baseline subtraction step that effectively removes the underlying heat capacity contribution to the DSC signal. The heat-flow signal must also be converted to units of the heater power (mW), rather than the more conventional mass-normalized units of W/g that some commercial instruments provide. A lateral shift of the temperature axis is also required by a subtraction of the onset melting temperature of the excess phase.

The adjusted heat flow curve, dQ/dt, is converted to dV_p/dr_p by

$$\frac{dV_p}{dr_p} = \frac{dQ}{dt}\frac{dt}{d(\Delta T)}\frac{d(\Delta T)}{dr_p}\frac{1}{m\Delta H_f(T)\rho(T)} \quad (24)$$

where $d(\Delta T)/dt$ is the scanning rate of the DSC experiment, m the mass of dry porous material, and $\Delta H_f(T)$ and $\rho(T)$ the temperature-dependent heat of fusion and density for the probe fluid, respectively. The expression has been modified slightly from a similar one presented by Ishikiriyama et al. [19]. The quantity $d(\Delta T)/dr_p$ is determined from the empirical expression in Eq. (22). Depending on whether a melting or freezing experiment is performed, the density at the start of the measurement is used, i.e., ρ_s (solid density) for a heating experiment, and ρ_l (liquid density) for a cooling experiment.

The pore size distributions with water as the pore fluid are shown in Figs. 21–23 for 7.5, 37.9, and 208.4 nm diameter CPG samples, in the same order. The following empirical equation for $\Delta H_f(T)$ is used [19,43].

$$\Delta H_f(T) = 334.1 + 2.119(T - T_m^0) - 0.00783(T - T_m^0)^2 \quad (25)$$

T_m^0 is the equilibrium melting temperature of water. Similarly, the empirical expressions for the density of water [19,44], ρ_{liq}, and ice [19,45], ρ_{sol}, are respectively

$$\rho_{liq}(T) = -7.1114 + 0.0882T - 3.1959 \times 10^{-4}T^2 + 3.8649 \times 10^{-7}T^3 \quad (26)$$

$$\rho_{sol}(T) = 0.917(1.032 - 1.17 \times 10^{-4}T) \quad (27)$$

where T is expressed in K. The thermoporometry-derived PSDs are, in general, modestly similar to those determined

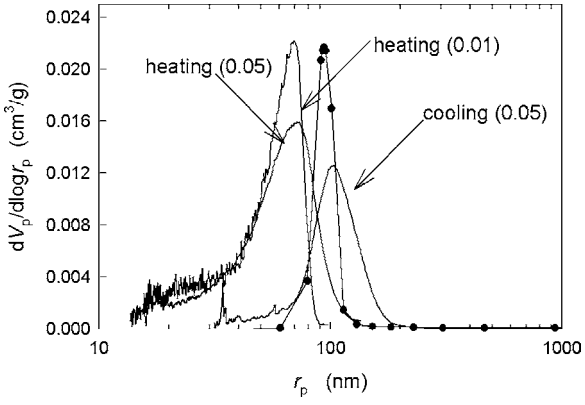

Fig. 23. Pore size distribution for 208.4 nm diameter CPG and water determined by thermoporometry (solid lines) and Hg intrusion (line with filled points). The Hg intrusion data are not plotted to scale with respect to the ordinate. DSC scan rates are noted in the figure (units: K/min).

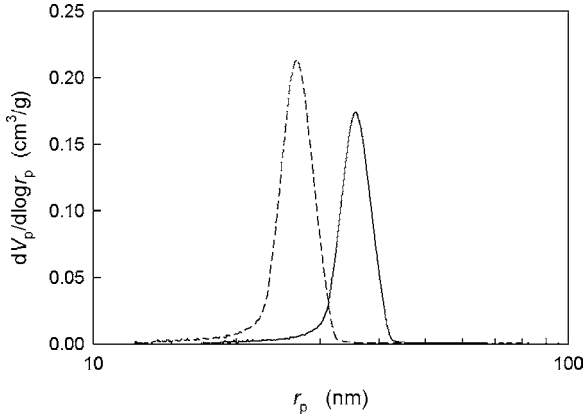

Fig. 24. PSD for 52.3 nm diameter CPG obtained from a water-freezing experiment. The dashed profile is generated with the empirical calibration expression from Eq. (17), while the solid curve is from Eq. (21), cited by Ishikiriyama et al. [19].

by mercury intrusion, whose distributions are also presented in these figures. For the majority of the CPG samples where the pore size distributions were calculated, the agreement between the heating and cooling experiments was reasonable, as seen in Figs. 21 and 22. The thermoporometry method was truly tested with the largest of the pores, namely the 208.4 nm diameter CPG sample shown in Fig. 23.

The empirical equations relating pore radius to temperature depression were presented previously, and a clear difference was noted between the experimental results in this study for melting (Eq. (16)) and freezing (Eq. (17)), and those reported by Ishikiriyama et al. [19], Eqs. (20) and (21), respectively. Recall that the latter equations were obtained from porous materials having pore sizes less than 10 nm radius, whereas the former are taken from samples with 3.75–104 nm radii. The effect of using either expression to transform a DSC curve into a size distribution is demonstrated in Fig. 24, where the calculated PSD from the freezing of water in 52.3 nm diameter CPG is displayed. The use of Eq. (21) dramatically shifts the pore size distribution from one having a maximum at $r_p = 26.5$ nm, i.e., pore diameter = 53.0 nm, in good agreement with the stated value, to a much larger size $r_p = 35.7$ nm (diameter = 71.4 nm). This difference emphasizes the importance of using calibration expressions derived from reference samples with similar pore sizes as the sample of interest.

Representative examples of the pore size distributions obtained with the organic liquids cyclohexane and chlorobenzene in controlled-pore glass are shown in Fig. 25, where they are compared against the PSD from water. These distributions are obtained in the same manner as for water, that is, from Eq. (24), with the exception that the temperature dependences for ρ_{liq}, ρ_{sol}, and ΔH_f are unknown. The values for these parameters over the entire temperature depression range are taken from Table 1. One set of distributions is given for heating (i.e., melting) experiments in a large pore sample,

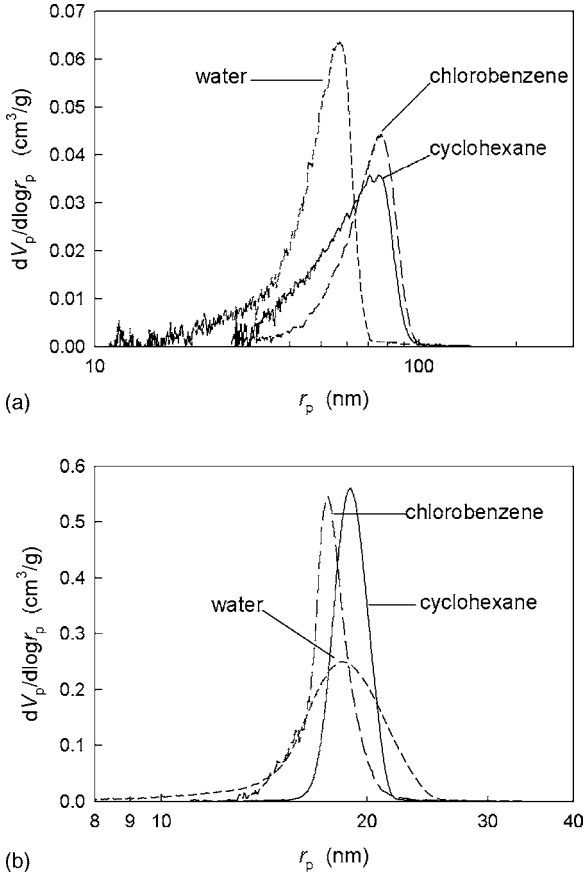

Fig. 25. Comparison of the pore size distributions with water, cyclohexane, and chlorobenzene as probe liquids. (a) Melting experiment for 127.3 nm diameter (63.65 nm radius) CPG. The peak maxima are at 57.0, 72.5, and 76.6 nm for water, cyclohexane, and chlorobenzene, respectively. (b) Freezing experiment for 37.9 nm diameter (18.95 nm radius) CPG. The peak maxima are at 18.3, 18.9, and 17.5 nm for water, cyclohexane, and chlorobenzene, respectively.

127.3 nm diameter (63.65 nm radius) CPG, in Fig. 25a. The organic liquids provide a similar measure of the pore size distribution versus water, although the peak maxima seem to indicate a larger pore radius than the nominal value: 72.5 nm from cyclohexane, and 76.6 nm from chlorobenzene. The peak pore radius from water is significantly lower at 57.0 nm. Similar underestimates are seen for water in the 101.0 and 208.4 nm CPG samples, a likely result of the smaller temperature depression of water, hence poorer melt peak separation for the excess melt peak, relative to the organic liquids. In Fig. 25b, the PSDs from freezing experiments in 37.9 nm diameter (18.95 nm radius) CPG are given for the same liquids. The pore radius from the peak maximum is at 18.3, 18.9, and 17.5 nm for water, cyclohexane, and chlorobenzene, respectively, in satisfactory agreement with each other.

3.5. Porosity parameters from pore size distribution

Once the pore size distribution is known, the total pore volume V_p, internal surface area S_p, and average pore radius

r_{ave} can be calculated as follows [20]

$$V_p = \int_0^\infty \left(\frac{dV_p}{dr_p}\right) dr_p \quad (28)$$

$$S_p = \int_0^\infty \frac{2}{r_p}\left(\frac{dV_p}{dr_p}\right) dr_p \quad (29)$$

$$r_{ave} = \frac{2V_p}{S_p} \quad (30)$$

For the purpose of this investigation, Eqs. (29) and (30) for the internal surface area and average pore radius assume a cylindrical pore shape. In the calculation of the total pore volume from Eq. (28), the non-freezable liquid adjacent to the pore walls is ignored.

Figs. 26–28 present a summary of the porosity parameters r_{ave}, V_p, and S_p, determined from the pore size distributions for chlorobenzene, water, and cyclohexane in the CPG samples. Because of the difficulty in preventing ambient moisture from interfering with the DSC thermograms in the dioxane/CPG mixtures, no results are reported for this combination. The results are compared to the porosity parameters measured by Hg intrusion porometry, as reported by the manufacturer in Table 2. The solid line in each plot represents a perfect correspondence between data from the two methods and is meant to guide the eye.

It is recognized that the pore size distributions for the porous glasses were obtained from parameters from Table 3, which were originally obtained from the same CPG samples. It should, therefore, be expected that the plots comparing the measured pore radii r_{ave}(PSD) to those from Hg intrusion should be in close agreement. This, in fact, is observed in Figs. 26a–28a, for the small and intermediate pore sizes, where the pore phase transition peaks are well removed from the bulk phase transition onset. The scatter increases with increasing pore radius because the experimental resolution for small temperature depressions leads to large uncertainties. Moreover, the method for separating the pore from the bulk signals was a simple truncation step. The overlap of the trailing edge of the bulk transition and the leading edge of the pore transition signals may not be properly represented.

The linear least-squares fits in the plots of the measured total pore volume V_p against the reference values provided by Hg intrusion are very reasonable, as seen by the dashed lines for chlorobenzene (slope = 1.14) and water (slope = 1.03) in Figs. 26b and 27b, respectively. The result for cyclohexane does not show as good agreement in Fig. 28b, where an apparent deviation is observed for the smallest pore volumes. There are several potential explanations for this trend. One scenario is that the non-polar cyclohexane may not be able to completely enter the smallest pores, for example, because of a lack of interaction with the polar silica pore walls. The polarity of chlorobenzene and water may lead to a more favorable interaction with the glass pore walls, allowing the liquid to better fill the pores. A second explanation is the result is due to ignoring any temperature dependence of the heat of fusion for cyclohexane. In fact, Mu and Malhotra [14] distinctly show that the enthalpy of melting transition for cyclohexane decreases with pore size. The trend appears to be the same as for water, therefore, the heat of fusion ΔH_f decreases with increasing temperature depression. The differential pore volume dV_p/dr_p is underestimated, causing a similar miscalculation of V_p. The concentration extrapolation method highlighted in Fig. 18 should resolve this question. Such a systematic approach was not done in this study. A further possibility that could explain the lack of agreement between V_p measured by thermoporometry and Hg intrusion is that the volume of any non-freezable liquid is ignored in Eqs. (24) and (28). This effect would produce the most serious underestimate for the smallest pore CPG, which indeed is the case for the cyclohexane result of Fig. 28b. However, the near 1-to-1 correspondences of V_p data for chlorobenzene (Fig. 26b) and water (Fig. 27b) suggest that the lack of agreement due to unaccounted non-freezable liquid is not significant.

The results in Figs. 26c–28c for the internal surface area S_p show an obvious overestimation, relative to the values suggested by nitrogen adsorption, by factors of 1.72, 1.73, and 2.02 for chlorobenzene, cyclohexane, and water, respectively. To arrive at the expression for S_p from the pore size distribution, cylindrical pore geometry was assumed, consistent with the observations for silica gels [20]. A cylindrical model provides the numerical constant 2 in Eq. (29). On the other hand, the BET method in nitrogen porometry does not postulate any particular pore geometry but does assume a cross-sectional area for a single nitrogen adsorbate molecule. Therefore, thermoporometry is useful for gauging the internal surface area of one porous material against another, but may not be suitable for determining an absolute measure.

3.6. Examples with other porous materials

3.6.1. Coatings with porous fillers

A coating having porous inorganic particles was prepared for investigation with thermoporometry. The coating contained 37.9 nm diameter CPG in a poly(vinyl alcohol) binder at a particle-to-binder weight ratio of 4:1. The nominal thickness was 100 μm on resin-coated paper, and water was used as the pore liquid. The heating and cooling DSC profiles are shown in Fig. 29a. Despite the thin coating and the small amount of porous solid contained within, the small endotherm peak on the low temperature side of the excess water melt transition (off scale in the figure) indicates that some of the liquid has entered the CPG pores. Similarly, a small exothermic peak is observed in the cooling signal that is consistent with the melt/freeze hysteresis in the porous solids (cf. Fig. 8).

From the DSC profiles, the pore size distribution of the porous particle within the coating is calculated using the transformation equations for the heat flow and temperature axes. The resulting PSD curve taken from a heating experiment is shown in Fig. 29b, and the distribution for the CPG alone is shown for comparison. A quantitative evaluation of

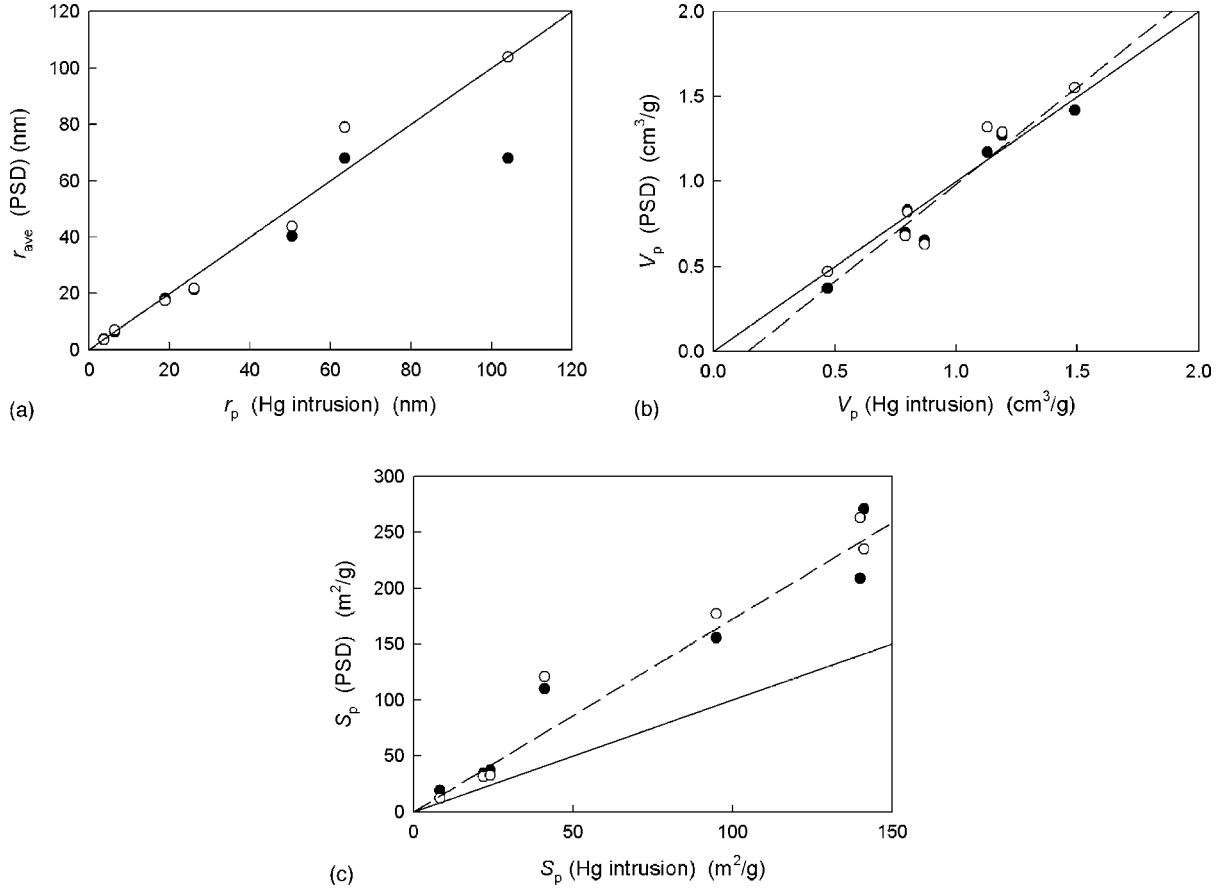

Fig. 26. Correlation plots showing the relationships between porosity parameters: (a) average pore radius r_{ave}, (b) total pore volume V_p, and (c) internal surface area S_p calculated from characteristic pore size distributions against values obtained from Hg intrusion, as cited in Table 2 for the system of chlorobenzene in CPG. The solid and open points are from heating and cooling experiments, in that order. The solid lines denote a one-to-one correspondence. The dashed lines in (b) and (c) are linear least-squares regression fits to the data with slopes of 1.14 and 1.72, respectively.

the total pore volume V_p and internal surface area S_p per unit area of the coating can be determined from the PSD. Instead of normalizing for the dry sample mass m in Eq. (24), the cross-sectional area of the paper disk is substituted. The pore volume in the coating was determined as 8.0 and 10.1 cm^3/m^2 in the heating and cooling experiments, respectively. The average pore radius r_{ave} for the example in Fig. 29b, is 11.6 nm, less than measured for the uncoated CPG (19.3 nm). A similar observation is noted from cooling experiments. One interpretation of a reduced pore radius is that the binder polymer might have occluded some of the larger pores and blocked water from entering. It is also important to note that thermoporometry is only measuring the amount of liquid taken up in the pores smaller than ca. 200 nm in radius. The technique does not account for water that the binder polymer or larger voids may absorb. In fact, one observation for this example, as well as others not reported here, is that the total endotherm area (pore + bulk melt) is often less than expected for the amount of water added to the sample. This indicates that some of the water is held in the hydrophilic binder polymer layer and does not undergo any phase transition and, therefore, does not contribute to the total pore volume as measured by thermoporometry.

Another application is shown in Fig. 30 for the melting of water in a coating that has fumed alumina as the porous filler in an undefined hydrophilic polymer binder. The pore size distribution compares favorably with the original alumina slurry in water, 40 wt.% solids. The average pore size in the coating from integrating the entire distribution is r_{ave} = 10.7 nm (distribution peak r_{max} = 10.7 nm), in good agreement with the pore size for the original alumina slurry from which the coating was prepared, r_{ave} = 9.9 nm (r_{max} = 10.4 nm). The total pore volume in the coating is measured to be 14.6 cm^3/m^2.

3.6.2. Porous and solid polymer microbeads

Many different compositions of polymeric microbeads have been investigated by thermoporometry, with a few shown in this report to demonstrate the flexibility of the technique. Both porous and solid particles have been investigated. Porous particles are thought to provide internal voids that allow for preferential adsorption of liquids or to affect the optical properties when used as addenda within a coated layer. Alternatively, solid particles of uniform size may pack to an extent that presents interstitial void space. It is noted that others have studied cross-linked polymer particles having porous

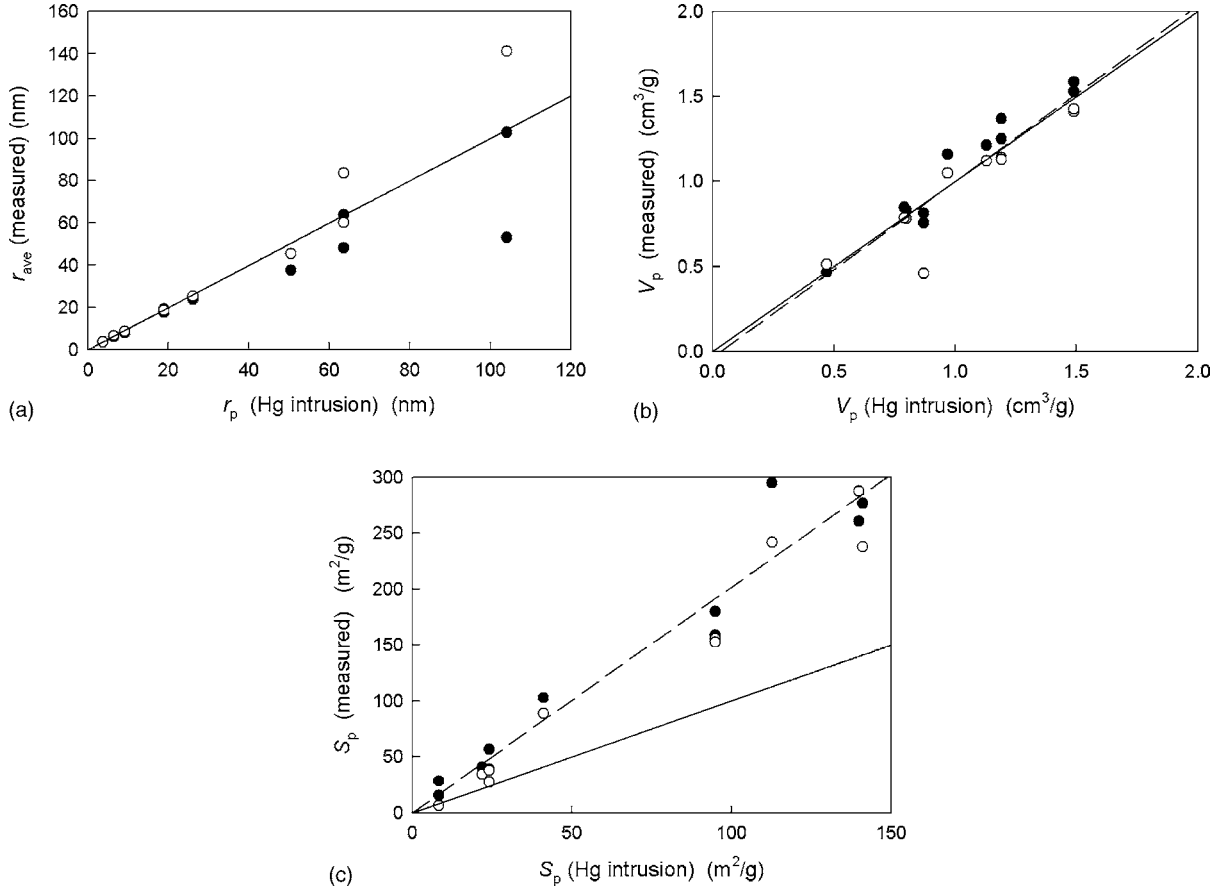

Fig. 27. Correlation plots of the porosity parameters for water in CPG, as explained in Fig. 26. The dashed lines in (b) and (c) are linear least-squares regression fits to the data with slopes of 1.03 and 2.02, respectively.

textures. Brun et al. [46] used benzene as the probe liquid in a cross-linked polymer resin, and water to probe the cavities in an anionic exchange resin [47]. Recently, thermoporometry has been applied by Wulff [15] to characterize porous polystyrene/divinylbenzene materials swollen with acetonitrile.

The first example is for a *porous*, highly cross-linked polymer bead of 100% ethylene glycol dimethacrylate, with a nominal diameter of 160 nm. The polymerization surfactant was removed from this sample prior to the thermoporometry measurement. As characterized previously by the BET method, the total pore volume V_p is 0.564 cm^3/g and an average pore radius r_{ave} = 5.0 nm. The inset in Fig. 31 shows the cooling and heating DSC profiles of a sample containing water as the pore-filling liquid. Distinct freezing and melting peaks are well separated from the off-scale equilibrium melting peak. The pore size distributions obtained from each cycle are shown in the main figure with reasonable overlap. From the cooling cycle, integration of the PSD according to Eq. (28) yields V_p = 0.501 cm^3/g and r_{ave} = 9.3 nm; the heating cycle gives V_p = 0.442 cm^3/g and r_{ave} = 7.9 nm. The thermoporometry results for the pore volume are similar, though slightly less, than those from the gas adsorption method. It is difficult to assess whether the pore size difference is due to possible swelling of the polymer particle by water, or if the temperature-to-radius calibration parameters from Table 3 and Eq. (22) are valid.

Continuing with the discussion on the same porous particle, there are two important details that are not captured in Fig. 31. The first is that thermoporometry strictly cannot distinguish between the internal pores and the interstitial pores, particularly if the sizes are comparable. This comment becomes significant in the next example. The second observation is that the total heat of fusion of water ΔH_f, pore plus excess phase, is less than expected for the same amount of water without any polymer. Several experiments were done with this porous bead, with the total ΔH_f implying that only 75–85% of the water freezes. The remainder is presumably held at the pore or outer particle surface or otherwise within the polymer matrix. We note that others have cited the presence of non-freezable water in polymers [47–49] because of a close association with the polymer through an ionic or hydrogen-bonding interaction. The presence of the glycol groups in this ethylene glycol dimethacrylate polymer bead likely adds some hydrophilic character that could inhibit freezing. Therefore, the total amount of water taken up by the sample is greater than represented by the total pore volume.

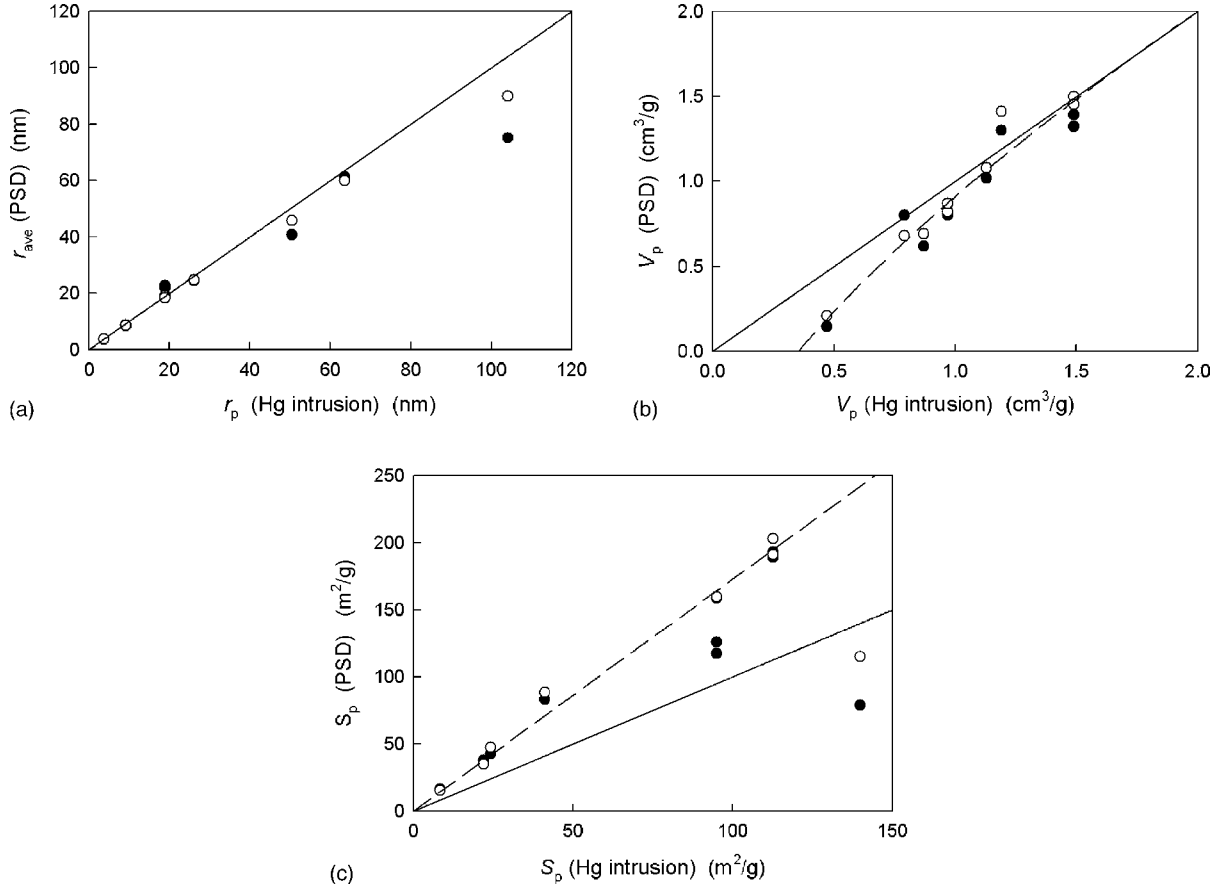

Fig. 28. Correlation plots of the porosity parameters for cyclohexane in CPG, as explained in Fig. 26. The dashed line in (b) is meant to guide the eye to the general trend of the data, and in (c), it is a linear least-squares regression fit with a slope of 1.73, minus the outliers to the far right.

The possibility of interstitial voids contributing to the measured porosity of polymer microbeads is demonstrated in Fig. 32. A 170 nm diameter *solid* particle of poly(methyl methacrylate-co-ethylene glycol dimethacrylate) with a quaternary ammonium salt as a particle stabilizer has been examined as a moist paste with water as the probe liquid. Presumably, this particle does not have internal pores, yet obvious freezing and melting peaks are observed by DSC, with the usual hysteresis associated with a porous material. From the pore size distribution, $V_p = 0.267\ cm^3/g$ and $r_{ave} = 7.95$ nm (heating branch) and $V_p = 0.232\ cm^3/g$ and $r_{ave} = 9.88$ nm (cooling). The water to dry bead weight ratio was 0.80 for this example. In Section 3.3, a method for determining the pore volume from the extrapolation of a liquid-to-solid concentration series was described (cf. Fig. 19). Fig. 33 provides the result for a similar extrapolation for water mixed with the solid polymer beads from six individual liquid-to-solid ratios. The extrapolation to zero excess water indicates a total pore volume of $0.39\ cm^3/g$, again consistent with the observation that these solid particles have an interstitial porosity. The linear nature of the extrapolation suggests that the particles are sufficiently aggregated, and their separation in the wet mixtures is independent of the amount of water present.

One last example of porous polymer beads is described for a porous aliphatic polyester copolymer with additional ionic character. Fig. 34 presents the PSD for a 355 nm diameter porous polyester bead in water with a water-to-bead weight ratio of 2.6. The average pore volume V_p from the heating and cooling cycles is $0.844\ cm^3/g$. The average pore radius r_{ave} from the distributions is 24.7 nm (heating) and 32.3 nm (cooling). The concentration extrapolation experiment is shown in Fig. 35, yielding a total pore volume V_p from the *x*-axis intercept at $0.854\ cm^3/g$, in excellent agreement. In general, it was observed that the thermoporometry method provided larger estimates of the pore volume than did nitrogen adsorption for many of the porous polyester particles, suggesting a preferred permeability of water over nitrogen, presumably because of the presence of the ionic comonomer. Non-freezable water is also present, which indicates additional water uptake by the polymer matrix.

4. Summary and conclusions

Thermoporometry is a calorimetric method that determines pore sizes from the melting or freezing point depression of a liquid confined in a pore, by reason of the added

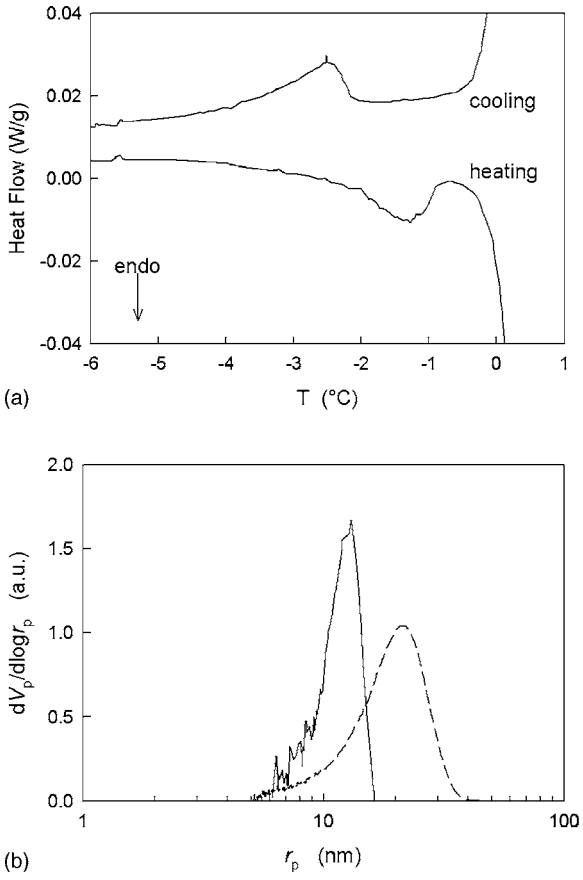

Fig. 29. (a) Heating and cooling DSC profiles for water in a 100 μm thick coating of 37.9 nm CPG in a polymer binder on paper. The heat-flow axis is greatly expanded to emphasize the small, but measurable, pore transitions. (b) Pore size distribution comparison of the CPG alone (dashed) and in the coating (solid). The distributions have been rescaled to fit on the same plot.

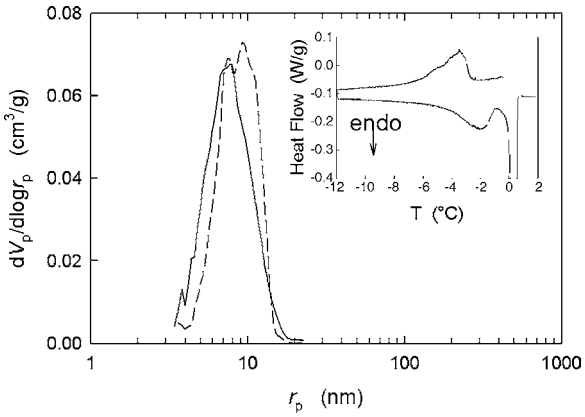

Fig. 31. The pore size distributions for 160 nm-diameter *porous* ethylene glycol dimethacrylate bead obtained upon cooling (dashed) and heating (solid). The inset figure shows the cooling (upper) and heating (lower) DSC profiles. Water is the pore-filling liquid.

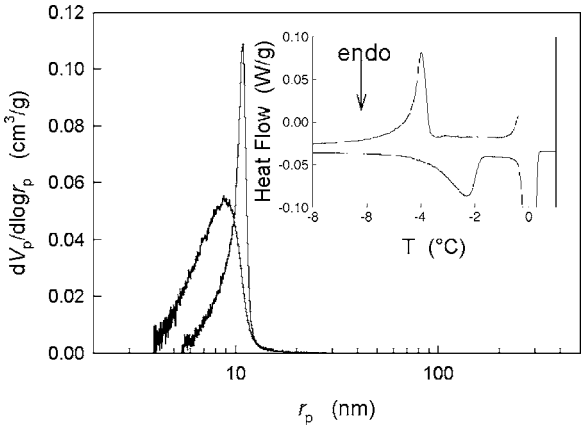

Fig. 32. The pore size distributions for a 170 nm diameter *solid* polymer bead obtained upon cooling (dashed) and heating (solid). The inset figure shows the cooling (upper) and heating (lower) DSC profiles. Water is the probe liquid.

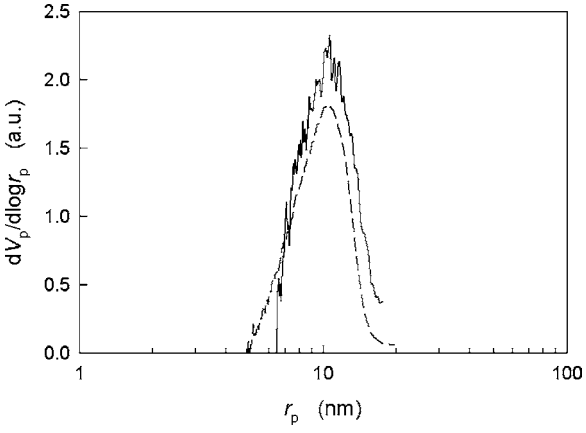

Fig. 30. Pore size distributions for a 40 wt.% slurry of fumed alumina (dashed line) and a handcoating with the same alumina held in a polymer binder layer (solid line). The curves have been rescaled for direct comparison.

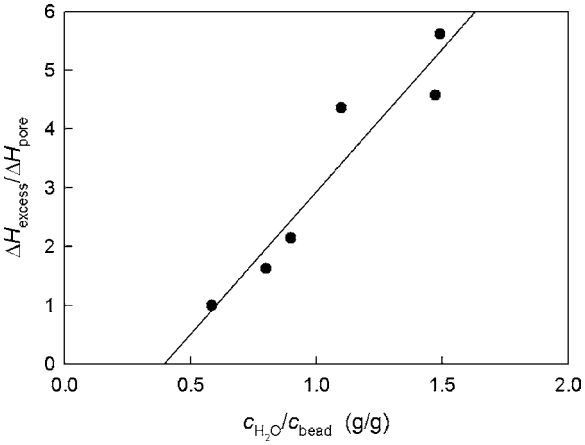

Fig. 33. The concentration series for water mixed with a *solid* polymer microbead. The ratio of the excess melt and pore melt areas, when extrapolated to the *x*-intercept, directly provides the total pore volume V_p as 0.39 cm^3/g.

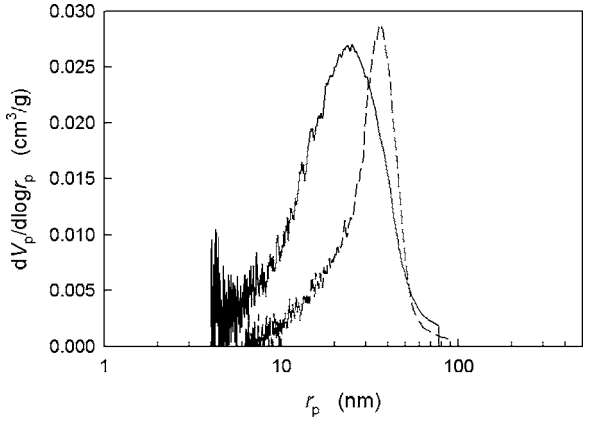

Fig. 34. The pore size distributions for a 355 nm diameter porous aliphatic polyester with ionic character bead obtained upon cooling (dashed) and heating (solid). Water is the probe liquid with a water-to-bead weight ratio of 2.6:1, and the average pore volume V_p from the two cycles is 0.844 cm^3/g.

contribution of surface curvature to the phase transition free energy. A summary of the theory behind the technique has been provided, as well as a thorough evaluation of the technique using a laboratory DSC instrument.

Optimum experimental conditions and data analysis protocols were determined from studies on mesoporous controlled-pore glass standards (CPG). Water, cyclohexane, chlorobenzene, and 1,4-dioxane were used as the pore-filling liquids. From the analysis of controlled-pore glass standards having radii in the range of 3.5–100 nm, a slow scanning rate of 0.05 K/min is advised, if water is the probe liquid, and approximately 2–5 times faster is acceptable for organic liquids. Small sample masses are also recommended (ca. 2–8 mg total weight). A recommendation is made for determining the temperature depression by using the difference between the pore melt peak maximum and the extrapolated bulk melt onset. This option proves to be the least sensitive to scanning rate and sample size. Procedures for obtaining total pore volume, specific surface area, pore radius, and ultimately pore size distribution are presented, with the latter comparing favorably with Hg intrusion data. The report concludes with applications on other porous materials, such as fumed alumina and porous organic microbeads. A demonstration of thermoporometry for detecting the pore structure in a coated layer is also reported.

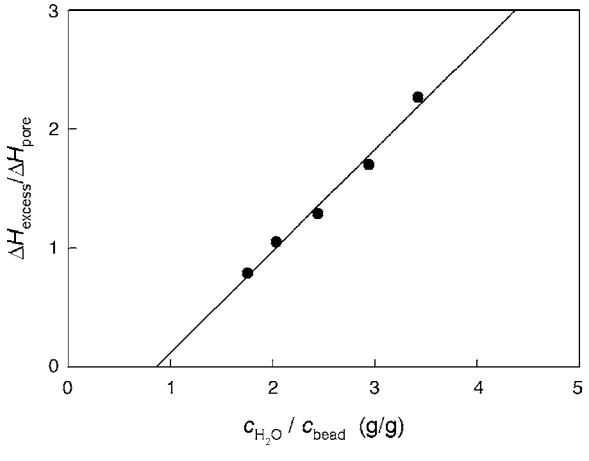

Fig. 35. The concentration series for water in the porous aliphatic polyester bead from the previous figure. The total pore volume V_p from the *x*-axis intercept is 0.854 cm^3/g.

It is also noted that thermoporometry has an approximate size limitation of 200 nm in radius with water as the probe liquid, increasing to 1000 nm for cyclohexane, so long as there is no interaction with the porous solid (e.g., swelling). Based on the observation with polymer microbeads, the technique does not account for liquid that the binder polymer may absorb and prevent from freezing. In fact, one observation is that the total endotherm area (pore + bulk melt) is often less than expected for the amount of water added to the sample. This indicates that some of the water is held in the hydrophilic binder polymer layer and does not undergo any phase transition and, therefore, does not contribute to the total pore volume as measured by thermoporometry. Finally, if interstitial pores are present, it may not be possible to differentiate between intraparticle and interparticle porosity contributions.

Acknowledgements

The CPG porosity standards were kindly supplied by E. Voll, who also provided some of the pore size distributions via mercury intrusion. The assistance of L. Franklin and C.J. Landry-Coltrain is acknowledged for the preparation of the hand-coated sample containing CPG as a porous filler. J. Leon, J. Kaeding, and R. Koestner provided the porous and solid polymer microbeads used in this study.

Appendix A

A.1. Derivation of pore size by gas adsorption

In order to determine a pore radius by gas adsorption, the Gibbs–Duhem equations for coexisting liquid and gas phases are introduced.

$$S_l\delta T - V_l\delta P_l + n_l\delta\mu_l = 0 \quad \text{(A.1)}$$

$$S_g\delta T - V_g\delta P_g + n_g\delta\mu_g = 0 \quad \text{(A.2)}$$

Eqs. (A.1) and (A.2) give the criteria for thermodynamic balance between the bulk gas and liquid phases external to the pores, i.e., where the interfacial area is flat. They relate chemical, thermal, and mechanical contributions, at equilibrium, upon infinitesimal changes in chemical potential $\delta\mu_i$, temperature δT, and pressure δP_i. Subscripts $i,j = gl$ for gas and liquid, and S_i, V_i, and n_i are the entropy, volume, and number of moles of phase i, respectively.

The nitrogen adsorption experiment is conducted at constant temperature ($\delta T = 0$) and under the condition that gaseous nitrogen is in equilibrium with its liquid phase, hence

$\delta\mu_g = \delta\mu_l = 0$. The Gibbs–Duhem equations reduce to

$$v_g \delta P_g = v_l \delta P_l \tag{A.3}$$

where the molar volumes of each phase ($v_i = V_i/n_i$) have been substituted. The Laplace equation (Eq. (1)) for a *hemispherical* surface, subject to incremental changes in pressure δP becomes

$$\delta P_g - \delta P_l = \delta\left(\frac{2\gamma_{gl}}{r}\right) \tag{A.4}$$

Keeping with convention, the phase with the higher pressure is on the convex side of the interface. Combining equations, one has

$$\delta\left(\frac{2\gamma_{gl}}{r}\right) = \left(\frac{v_l - v_g}{v_l}\right)\delta P_g = -\frac{RT}{v_l}\frac{\delta P_g}{P_g} \tag{A.5}$$

where $v_l \ll v_g$, and ideal gas behavior, that is $v_g = RT/P_g$, has been assumed. Integration of Eq. (A.5) from P_g^0 at $r = \infty$ to P_g at $r = r$ gives

$$\ln\left(\frac{P_g}{P_g^0}\right) = -\frac{2\gamma_{gl} v_l}{rRT} \tag{A.6}$$

A.2. Melt/freeze temperature shift for coexisting solid and liquid

The Gibbs–Duhem equations describe the balance between mechanical, thermal, and chemical potential contributions at equilibrium for a planar system of coexisting bulk phases [7]:

$$S_s \delta T - V_s \delta P_s + n_s \delta\mu_s = 0 \tag{A.7}$$

$$S_l \delta T - V_l \delta P_l + n_l \delta\mu_l = 0 \tag{A.8}$$

$$S_g \delta T - V_g \delta P_g + n_g \delta\mu_g = 0 \tag{A.9}$$

Eqs. (A.7)–(A.9) are supplemented with the Laplace equations (A.10)–(A.12) to account for curved interfaces between liquid/solid (l/s), liquid/gas (l/g), and solid/gas (s/g) bulk phases:

$$P_l - P_g = \gamma_{lg}\frac{dA_{lg}}{dV_l} \tag{A.10}$$

$$P_g - P_s = \gamma_{gs}\frac{dA_{gs}}{dV_g} \tag{A.11}$$

$$P_s - P_l = \gamma_{sl}\frac{dA_{sl}}{dV_s} \tag{A.12}$$

With the Gibbs phase rule indicating two critical surfaces, one may choose the gas–liquid and gas–solid interfaces. Upon differentiation, Eqs. (A.10) and (A.11) become

$$\delta P_l - \delta P_g = \delta\left(\gamma_{gl}\frac{dA_{gl}}{dV_l}\right) \tag{A.13}$$

$$\delta P_g - \delta P_s = \delta\left(\gamma_{gs}\frac{dA_{gs}}{dV_g}\right) \tag{A.14}$$

The derivation continues with the subtraction of Eq. (A.8) from (A.9), and Eq. (A.7) from (A.9) for the two interfaces (molar volumes $v_i = V_i/n_i$ and entropies $s_i = S_i/n_i$)

$$\left(\frac{s_g - s_l}{v_g - v_l}\right)\delta T = \frac{v_g}{v_g - v_l}\delta P_g - \frac{v_l}{v_g - v_l}\delta P_l \quad \text{(gas–liquid)} \tag{A.15}$$

$$\left(\frac{s_g - s_s}{v_g - v_s}\right)\delta T = \frac{v_g}{v_g - v_s}\delta P_g - \frac{v_s}{v_g - v_s}\delta P_s \quad \text{(gas–solid)} \tag{A.16}$$

A second subtraction of Eq. (A.15) from (A.16) and substitution for δP_l and δP_s from Eqs. (A.13) and (A.14), respectively, gives

$$\left[\left(\frac{s_g - s_s}{v_g - v_s}\right) - \left(\frac{s_g - s_l}{v_g - v_l}\right)\right]\delta T = \frac{v_s}{v_g - v_s}\delta\left(\gamma_{gs}\frac{dA_{gs}}{dV_g}\right) + \frac{v_l}{v_g - v_l}\delta\left(\gamma_{gl}\frac{dA_{gl}}{dV_l}\right) \tag{A.17}$$

Let us assume cylindrical pores with hemispherical surfaces. Furthermore, we note that $v_g \gg v_l$, $v_g \gg v_s$ and

$$\left(\frac{dA_{ij}}{dV_j}\right) = \frac{2}{r} \quad \text{(concave toward phase } j\text{)} \tag{A.18}$$

$$\left(\frac{dA_{ij}}{dV_j}\right) = -\frac{2}{r} \quad \text{(concave toward phase } i\text{)} \tag{A.19}$$

Thus, for the picture represented in Fig. 2.

$$(s_l - s_s)\delta T = -2\left[v_s\delta\left(\frac{\gamma_{gs}}{r_{gs}}\right) + v_l\delta\left(\frac{\gamma_{gl}}{r_{gl}}\right)\right] \tag{A.20}$$

For the temperature interval of interest, let us assume entropy change $s_l - s_s$, surface tensions γ_{gs}, γ_{gl}, and specific volumes v_s, v_l are constant. Therefore,

$$(s_l - s_s)T = \Delta h_f \tag{A.21}$$

$$\frac{\delta T}{T} = -\frac{2}{\Delta h_f}\left[v_s\gamma_{gs}\delta\left(\frac{1}{r_{gs}}\right) + v_l\gamma_{gl}\delta\left(\frac{1}{r_{gl}}\right)\right] \tag{A.22}$$

where Δh_f is the molar heat of fusion. The effect of the radius of curvature of the two interfaces on the equilibrium melting/freezing temperature T_0 is determined by an integration from $1/r_{gs} = 0$ and $1/r_{gls} = 0$ at $T = T_0$ (i.e., flat interfaces) to the arbitrary values $1/r_{gs}$ and $1/r_{gl}$ at the temperature of interest T to give

$$\ln\left(\frac{T}{T_0}\right) = -\frac{2}{\Delta h_f}\left(\frac{v_l\gamma_{gl}}{r_{gl}} + \frac{v_s\gamma_{gs}}{r_{gs}}\right) \tag{A.23}$$

Morioka et al. [50] cite a similar expression for coexisting solid and liquid adsorbate in a porous solid, with the exception of a sign change for one of the terms in parenthesis on the right-hand side of Eq. (A.23). A reversal of the curvature of either the solid/vapor or liquid/vapor meniscus in Fig. 2 remedies this difference.

A.3. Melt/freeze temperature shift for saturated pore

To derive the phase transition temperature–pore size relationship for the case of a saturated porous solid, one can consider the solid–liquid and gas–solid interfaces when subtracting the Gibbs–Duhem equations. Following the logic of Eqs. (A.15)–(A.17), one arrives at

$$\left[\left(\frac{s_s - s_g}{v_s - v_g}\right) - \left(\frac{s_l - s_s}{v_l - v_s}\right)\right]\delta T = \frac{-v_g}{v_s - v_g}\delta\left(\gamma_{gs}\frac{dA_{gs}}{dV_g}\right) + \frac{v_l}{v_l - v_s}\delta\left(\gamma_{sl}\frac{dA_{sl}}{dV_s}\right) \quad (A.24)$$

For the hemispherical solid–liquid surface $dA_{sl}/dV_s = 2/r_{sl}$, and for the planar gas–solid surface, $dA_{gs}/dV_g = 0$. If we, again, assume $v_g \gg v_l$, v_s as well as $v_g \gg v_l - v_s$, one has

$$(s_l - s_s)\delta T = -2v_l\gamma_{sl}\delta\left(\frac{1}{r_{sl}}\right) \quad (A.25)$$

Upon substitution of the molar entropy difference $s_l - s_s$, according to Eq. (A.21) and integration from T_0 to T for the transition from a flat to curved solid–liquid interface, the simple thermoporometry relationship is obtained (assuming constant Δh_f, v_l, and γ_{sl})

$$\ln\frac{T}{T_0} = -\frac{2v_l\gamma_{sl}}{\Delta h_f r_{sl}} \quad (A.26)$$

Brun et al. [6] have numerically evaluated Eq. (A.25) to arrive at an expression for the solidification entropy change, $s_l - s_s$, by reason that a large temperature depression of up to 40 K for water (and 60 K for benzene) was studied. Empirical expressions for temperature-dependent heat capacities and specific volumes were incorporated into the integration to arrive at an empirical expression for the freezing-point depression and pore radius (see Eqs. (18) and (19)).

References

[1] K.S.W. Sing, D.H. Everett, R.A.W. Haul, L. Moscou, R.A. Pierotti, J. Rouquérol, T. Siemieniewska, Pure Appl. Chem. 57 (1985) 603.
[2] K. Kaneko, J. Membr. Sci. 96 (1994) 59.
[3] K. Sakai, J. Membr. Sci. 96 (1994) 91.
[4] S.-I. Nakao, J. Membr. Sci. 96 (1994) 131.
[5] D.R. Milburn, B.D. Adkins, B.H. Davis, in: F. Rodriguez-Reinoso, et al. (Eds.), Characterization of Porous Solids, vol. II, Elsevier Science Publishers B.V., Amsterdam, 1991, pp. 543–551.
[6] M. Brun, A. Lallemand, J.-F. Quinson, C. Eyraud, Thermochim. Acta 21 (1977) 59.
[7] R. Defay, I. Prigogine, A. Bellemans, D.H. Everett, Surface Tension and Adsorption, Wiley, New York, 1966.
[8] G.K. Rennie, J. Clifford, J. Chem. Soc., Faraday Trans. I 73 (1977) 680.
[9] K. Ishikiriyama, M. Todoki, Thermochim. Acta 256 (1995) 213.
[10] K. Morishige, K. Kawano, J. Chem. Phys. 110 (1999) 4867.
[11] G.E. Romanos, V. Kasselouri, K. Beltsios, N.K. Kanellopoulos, J. Therm. Anal. Calorim. 73 (2003) 183.
[12] C.L. Jackson, G.B. McKenna, J. Chem. Phys. 93 (1990) 9002.
[13] M. Sliwinska-Bartkowiak, J. Gras, R. Sikorski, R. Radhakrishnan, L. Gelb, K.E. Gubbins, Langmuir 15 (1999) 6060.
[14] R. Mu, V.M. Malhotra, Phys. Rev. B 44 (1991) 4296.
[15] M. Wulff, Thermochim. Acta 419 (2004) 291.
[16] M. Baba, J.-M. Nedelec, J. Lacoste, J.-L. Gardette, M. Morel, Polym. Degrad. Stab. 80 (2003) 305.
[17] J. Warnock, D.D. Awschalom, M.W. Shafer, Phys. Rev. Lett. 57 (1986) 1753.
[18] K.M. Unruh, T.E. Huber, C.A. Huber, Phys. Rev. B 48 (1993) 9021.
[19] K. Ishikiriyama, M. Todoki, K. Motomura, J. Colloid Interface Sci. 171 (1995) 92.
[20] K. Ishikiriyama, M. Todoki, J. Colloid Interface Sci. 171 (1995) 103.
[21] E.W. Hansen, H.C. Gran, E.J. Sellevold, J. Phys. Chem. B 101 (1997) 7027.
[22] K. Lewandowski, F. Svec, J.M.J. Frechet, J. Appl. Polym. Sci. 67 (1998) 597.
[23] J.E. Kaeding, J.W. Leon, C.J. Landry-Coltrain, A.R. Pitt, T.J. Wear, G.E. Missell, D.E. Smith, US Patent Appl. Publication No. US 2003/0198761 A1 (October 23, 2003).
[24] Handbook of Chemistry, Physics, 57th ed., CRC Press, Cleveland, 1976.
[25] M.K. Titulaer, J.C. van Miltenburg, J.B.H. Jansen, J.W. Geus, Recl. Trav. Chim. Pays-Bas 114 (1995) 361.
[26] J.N. Hay, P.R. Laity, Polymer 41 (2000) 6171.
[27] L.G. Homshaw, J. Colloid Interface Sci. 84 (1981) 141.
[28] M. Iza, S. Woerly, C. Danumah, S. Kaliaguine, M. Bousmina, Polymer 41 (2000) 5885.
[29] A. Schreiber, I. Ketelsen, G.H. Findenegg, Phys. Chem. Chem. Phys. 3 (2001) 1185.
[30] J.H. Strange, M. Rahman, E.G. Smith, Phys. Rev. Lett. 71 (1993) 3589.
[31] T. Takamuku, M. Yamagami, H. Wakita, Y. Masuda, T. Yamaguchi, J. Phys. Chem. B 101 (1997) 5730.
[32] Y.P. Handa, M. Zakrzewski, C. Fairbridge, J. Phys. Chem. 96 (1992) 8594.
[33] E. Molz, A.P.Y. Wong, M.H.W. Chan, J.R. Beamish, Phys. Rev. B 48 (1993) 5741.
[34] J.L. Tell, H.J. Maris, Phys. Rev. B 28 (1983) 5122.
[35] M. Sliwinska-Bartkowiak, G. Dudziak, R. Sikorski, R. Gras, R. Radhakrishnan, K.E. Gubbins, J. Chem. Phys. 114 (2001) 950.
[36] J.A. Duffy, N.J. Wilkinson, H.M. Fretwell, M.A. Alam, R. Evans, J. Phys.: Condens. Matter 7 (1995) 713.
[37] J.-C. Li, D.K. Ross, M.J. Benham, J. Appl. Crystallogr. 24 (1991) 794.
[38] A.A. Antoniou, J. Phys. Chem. 68 (1964) 2754.
[39] R.T. Pearson, W. Derbyshire, J. Colloid Interface Sci. 46 (1974) 232.
[40] S. Stapf, R. Kimmich, J. Chem. Phys. 103 (1995) 2247.
[41] B.V. Enüstün, H.S. Sentürk, O. Yurdakul, J. Colloid Interface Sci. 65 (1978) 509.
[42] R. Denoyel, R.J. Pellenq, Langmuir 18 (2002) 2710.
[43] Randall, International Critical Tables V–VII, McGraw-Hill, New York, 1930.
[44] D.E. Hare, C.M. Sorensen, J. Chem. Phys. 84 (1986) 5085.
[45] S. Fukusako, Int. J. Thermophys. 11 (1990) 353.
[46] M. Brun, J.-F. Quinson, R. Spitz, M. Bartholin, Makromol. Chem. 183 (1982) 1523.
[47] J.-F. Quinson, M. Brun, R. Spitz, M. Bartholin, Makromol. Chem. 185 (1984) 1105.
[48] S.P. Rowland (Ed.), Water in Polymers, ACS Symposium Series No. 127, American Chemical Society, Washington, 1980.
[49] K. Ishikiriyama, M. Todoki, J. Polym. Sci. B: Polym. Phys. 33 (1995) 791.
[50] Y. Morioka, J. Kobayashi, I. Higuchi, J. Colloid Interface Sci. 42 (1973) 156.
[51] M. Renaud, R. Fourme, J. Chim. Phys. 63 (1966) 27.
[52] S.G. Biswas, Acta Cryst. 11 (1958) 882.